ISSN 2543-9901

JOURNAL OF CASTING & MATERIALS ENGINEERING

AGH UNIVERSITY OF KRAKOW
FACULTY OF FOUNDRY ENGINEERING

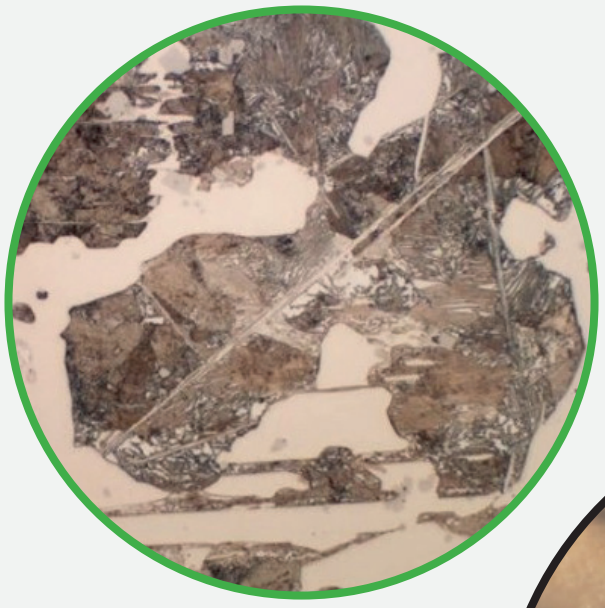

QUARTERLY
Vol. 9 No. 4/2025

JCME

AGH UNIVERSITY PRESS
KRAKOW 2025

www:
https://journals.agh.edu.pl/jcme/

AGH UNIVERSITY PRESS KRAKOW 2025

Wydawnictwa AGH (AGH University Press)
al. A. Mickiewicza 30, 30-059 Kraków
tel. 12 617 32 28, 12 638 40 38
e-mail: redakcja@wydawnictwoagh.pl
http://www.wydawnictwa.agh.edu.pl

Contents

Journal of Casting & Materials Engineering Vol. 9 No. 4 (2025) 50–58
https://doi.org/10.7494/jcme.2025.9.4.50

Influence of the Addition of Tellurium and Heat Treatment on the Microstructure of Hypoeutectic White Cast Iron

Alicja Trela-Przybyło[1,*], Magdalena Kawalec[1], Marcin Górny[1]

[1] AGH University of Krakow, Faculty of Foundry Engineering, 23 Reymonta St., 30-059 Krakow, Poland
**e-mail:atp@agh.edu.pl.pl*

Received: 16 July 2025/Accepted: 14 November 2025/Published online: 23 December 2025.
This article is published with open access at AGH University of Science and Technology Journals.

Abstract

This study investigates how the addition of tellurium and heat treatment affects the microstructure of hypoeutectic white cast iron that has been modified with alloying elements such as titanium, chromium and vanadium. Samples with different chemical compositions were prepared and subjected to a two-step heat treatment process. Microstructural characterisation was performed using optical and scanning electron microscopy. The results show that introducing tellurium significantly affects the morphology of the cementite and carbide phases, causing them to fragment and become more evenly distributed. Furthermore, heat treatment enhanced matrix refinement and promoted phase stability. The combination of tellurium addition and heat treatment produced the most favourable microstructures, characterised by the high dispersion of hard phases within a fine-grained matrix.

Keywords:

microstructure, white cast iron, heat treatment, hypoeutectic white cast iron, tellurium

1. INTRODUCTION

White cast irons are widely valued for their excellent hardness and wear resistance, primarily due to the presence of hard carbide phases within their microstructure. To further enhance these properties for specific engineering applications, alloying elements and heat treatments are commonly employed. Among the various alloying elements, titanium (Ti), chromium (Cr), and vanadium (V) are known to refine the microstructure, promote carbide formation, and significantly improve overall hardness and abrasion resistance [1]. While less extensively studied in cast irons, tellurium (Te) has recently garnered interest due to its potential to modify solidification behavior and influence the morphology of eutectic carbides and graphite phases [2, 3]. Tellurium acts as a surface-active element that can affect nucleation and growth mechanisms during solidification, potentially leading to improved material performance [2, 3].

Concurrently, heat treatment remains a highly effective method for tailoring the microstructure of cast alloys. By precisely controlling heating rates, holding temperatures, and cooling conditions, significant changes can be achieved in the phase composition, matrix structure, and mechanical properties of cast irons. The synergistic combination of alloying and heat treatment offers a powerful approach to customize material behavior for diverse engineering applications.

The microstructure of classic hypoeutectic white cast irons is primarily governed by their chemical composition, cooling rate, and the presence of alloying additives or modifiers. In hypoeutectic structures, the main microstructural constituents are primary cementite (Fe_3C), ledeburitic eutectic, and a matrix that can be pearlitic, austenitic, or martensitic depending on the heat treatment conditions [4, 5]. Cementite typically forms needle-like or plate-like precipitates, often creating continuous networks along grain boundaries. In high-chromium cast irons, the presence of M_7C_3-type carbides is also observed, which contribute to greater hardness and abrasion resistance but can also increase material brittleness [4–6].

In alloyed cast irons with additions of Ti, Cr, or V, additional carbides such as TiC, VC, and Cr_7C_3 may precipitate, primarily in inter-dendritic zones, appearing as bright particles with varied morphologies [5, 7]. The specific phase system and size of these carbides depend on element concentration and solidification parameters. Directional cooling can lead to the orientation of precipitates in accordance with the temperature gradient, potentially resulting in anisotropic material properties [4]. Without modification, significant grain size and uneven distribution of hard phases are often observed in the microstructure [3, 8].

Previous research has highlighted tellurium as a promising modifier in aluminum and steel alloys, demonstrating its ability to alter eutectic morphologies, reduce dendrite arm spacing, and modify inclusion behavior [3, 9]. For instance, studies on Al-Si alloys have shown that Te can effectively transform sharp, plate-like intermetallics into more compact, rounded forms, thereby enhancing microstructural uniformity and stability during thermal cycles [10]. However, the specific role of tellurium in cast irons, especially

when combined with complex alloying systems and subsequent heat treatment, remains largely underexplored.

This research aims to address this knowledge gap by systematically evaluating the influence of the addition of tellurium on the microstructure of hypoeutectic white cast iron, both with and without supplementary alloying elements (Ti, Cr, and V), and critically, both before and after a specific heat treatment process. The study focuses on key microstructural features such as carbide morphology, dendritic structure (quantified by Secondary Dendrite Arm Spacing – SDAS), inclusion formation, and matrix transformations. The overarching goal is to elucidate the mechanisms by which tellurium modifies solidification and phase evolution in these complex cast iron systems. Notably, SDAS is a critical parameter that reflects casting microstructure quality, as it correlates strongly with structural homogeneity, phase precipitate distribution, and segregation tendencies [11]. A reduction in SDAS, as observed with tellurium additions in other alloys [3], indicates a finer and more homogeneous microstructure due to increased nucleation frequency and intensified crystallization.

2. METHODOLOGY

This study investigated the influence of tellurium (Te) addition and heat treatment on the microstructure of hypoeutectic white cast iron, both in its base form and when alloyed with titanium (Ti), chromium (Cr), and vanadium (V). Thermal analysis cups, pre-dosed with tellurium paste at the base, were utilized as the tellurium source. These cups were first filled with the base cast iron melt and subsequently served as the mechanism for introducing the tellurium into the alloy during the experiment, a method intended to enhance tellurium recovery in the tested samples.

2.1. Sample preparation and chemical composition

A series of samples were prepared with different chemical compositions to systematically evaluate the effects of the alloying elements and tellurium. The designations for the samples are as follows:

- **W0:** Baseline white cast iron (no alloying additives).
- **W0T:** Baseline white cast iron with tellurium addition (One Tellurium Thermal Analysis Cup).
- **W1:** Baseline cast iron with titanium addition (3% Fe-Ti by weight of the charge).
- **W1T:** Baseline cast iron with titanium and tellurium addition (Alloy W1 plus one Tellurium Thermal Analysis Cup).
- **W2:** Baseline cast iron with titanium and chromium additions (3% Fe-Ti; 3.5% Fe-Cr by weight of the charge).
- **W2T:** Baseline cast iron with titanium, chromium, and tellurium additions (Alloy W2 plus one Tellurium Thermal Analysis Cup).
- **W3:** Baseline cast iron with titanium, chromium, and vanadium additions (3% Fe-Ti; 3.5% Fe-Cr; 0.2% Fe-V by weight of the charge).
- **W3T:** Baseline cast iron with titanium, chromium, vanadium, and tellurium additions (Alloy W3 plus one Tellurium Thermal Analysis Cup).

The chemical compositions of the W0, W1, W2, and W3 samples are detailed in Table 1, showing the weight percentages of carbon (C), silicon (Si), phosphorus (P), sulfur (S), chromium (Cr), titanium (Ti), and vanadium (V).

Table 1
Chemical composition of samples W0, W1, W2 and W3

Sample number	Chemical composition [wt. %]						
	C	Si	P	S	Cr	Ti	V
W0	3.050	0.078	0.040	0.014	0.038	0.003	<0.001
W1	2.860	0.085	0.043	0.015	0.035	1.560	0.048
W2	3.000	0.152	0.045	0.017	2.710	1.560	0.056
W3	3.020	0.177	0.047	0.017	2.950	1.010	0.220

2.2. Microstructural characterisation

Microstructural investigations were performed using two primary techniques:

- Optical Microscopy: A Leica MEF4M optical microscope, coupled with a computer and Leica Qwin software, was used for general microstructural observations and for measuring structural parameters. All optical micrographs were taken at a magnification of 500×.
- Scanning Electron Microscopy (SEM): A JEOL 5500VL scanning electron microscope was utilized for more detailed microstructural analysis and to identify crystallized phases. All SEM micrographs were taken at a magnification of 1500×.

A key quantitative parameter determined during the study was the Secondary Dendrite Arm Spacing (SDAS). SDAS was measured at a magnification of 200× to assess the homogeneity and fineness of the dendritic structure. Figure 1 presents the scheme for determining the SDAS parameter. Note that for samples W0 and W1 after heat treatment, dendrites were not observed, preventing SDAS determination for these specific cases.

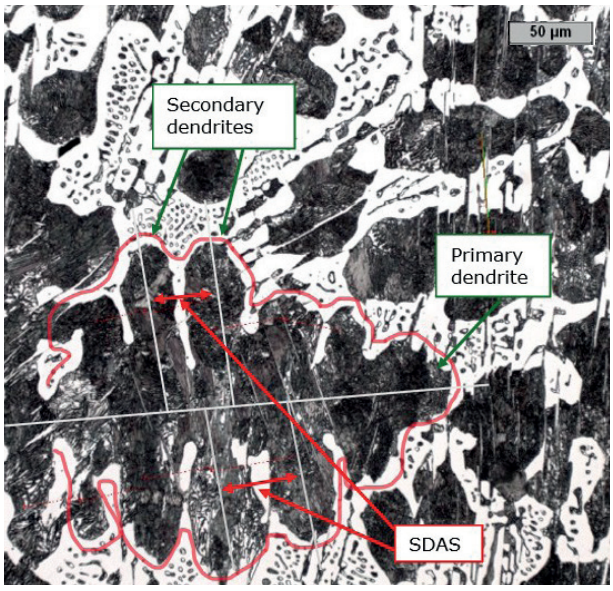

Fig. 1. Examples of determining the SDAS coefficient

2.3. Heat treatment process

Selected samples underwent a two-step heat treatment process to investigate its impact on microstructure. The scheme of the conducted heat treatment is presented in Figure 2.

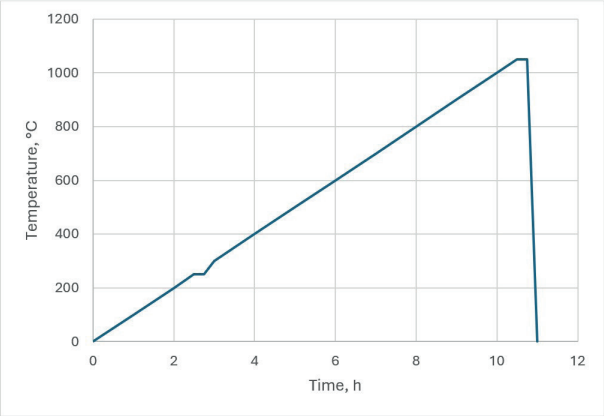

Fig. 2. Heat treatment scheme

The heat treatment procedure was carried out using a Czylok FCF 22H chamber furnace.

The samples were placed inside the furnace at room temperature (RT). The heating cycle involved the following stages:

- Stage 1 (Initial Heating): The samples were heated together with the furnace at a rate of 100°C/h up to a temperature of 250°C.
- Stage 2 (First Hold): The samples were held at 250°C for 15 minutes.
- Stage 3 (Main Heating): The temperature was again increased at a rate of 100°C/h until the final annealing temperature of 1050°C was reached.
- Stage 4 (Second Hold/Annealing): The samples were held at 1050°C for 15 minutes.
- Stage 5 (Cooling): Following the annealing stage, the samples were subjected to water quenching.

Samples subjected to heat treatment were designated with the suffix "_OC" (e.g., W0_OC, W0T_OC, W1_OC, W1T_OC, etc.).

The combined approach of different chemical compositions, applying a controlled heat treatment, and employing advanced microscopic techniques allowed for a comprehensive analysis of the influence of tellurium addition and heat treatment on the microstructure of hypoeutectic white cast iron.

3. RESULTS

The microstructures obtained during melting and after subsequent heat treatments are presented in Figures 3–6. During microscopic observations, given the appearance of various carbides in the structure, the primary focus was on analyzing their potential influence on the abrasion resistance of the obtained alloys.

Figure 3 displays the microstructures of the baseline samples (W0, W0T, W0_OC, W0T_OC). The reference sample (W0) exhibited secondary ledeburite with visible plates of ferrite cementite embedded within an austenitic matrix. The cementite formed a continuous, web-like structure. The addition of tellurium (W0T) to the reference sample resulted in a distinct fragmentation and rounding of these cementite plates. Conversely, the application of heat treatment (W0_OC) led to further fragmentation of the cementite and a transformation of the austenitic matrix into a martensitic phase. The combination of tellurium addition and heat treatment (W0T_OC) yielded the most favorable microstructure among all baseline variants, characterized by the highest level of homogeneity and stability. This was achieved by inhibiting the transformation of austenite into martensite and preventing the dissolution of carbides.

Figure 4 illustrates the microstructures of the samples containing titanium (W1, W1T, W1_OC, W1T_OC). In sample W1 (with Ti addition), bright TiC carbide inclusions were visible, primarily located at the grain boundaries. Their presence caused fragmentation of the structure and partial modification of the cementite shape. With the presence of tellurium (W1T), the distribution of TiC phases became more uniform, and the morphology of cementite was further altered. Sample W1_OC (Ti with heat treatment) exhibited a finer matrix structure and less continuous secondary cementite. The sample designated W1T_OC (Ti, Te with heat treatment) was characterized by a homogeneous phase distribution and highly fragmented cementite.

Figure 5 shows the microstructures of samples containing titanium and chromium (W2, W2T, W2_OC, W2T_OC). The addition of chromium to sample W2 resulted in the formation of additional elongated Cr_7C_3-type carbides, visible as bright, sharp-edged needles in the microstructure, which is typical for high-chromium cast irons [12]. In the sample identified as W2T (Ti + Cr + Te), the presence of tellurium led to shortened, rounded Cr_7C_3 carbides and fragmented cementite. Sample W2_OC (Ti + Cr with heat treatment) exhibited carbide phases with a more regular morphology, accompanied by fragmented secondary cementite. W2T_OC (Ti + Cr + Te with heat treatment) displayed a structure characterized by fine and uniformly distributed Cr_7C_3 and TiC carbides. It was observed that tellurium effectively reduced the length of needle-like Cr_7C_3 carbides, improving their morphology, while heat treatment fragmented the matrix and increased martensite content.

Figure 6 presents the microstructures of samples containing titanium, chromium, and vanadium (W3, W3T, W3_OC, W3T_OC). W3 showed a fine-grained structure with VC phases, consistent with existing literature on the influence of V on cast irons. Subsequent optimization of the microstructure and increased homogeneity of phase distribution were observed. In the case of sample W3T (Ti + Cr + V + Te), the presence of tellurium was found to impede the agglomeration of VC carbides, thereby facilitating their more even distribution. The phase composition of W3_OC (Ti + Cr + V with heat treatment) was characterized by the presence of fragmented cementite along with an ordered matrix structure. The W3T_OC sample (Ti + Cr + V + Te with heat treatment) demonstrated a structure with a high degree of fragmentation of carbide phases (TiC, Cr_7C_3, VC) and their uniform distribution.

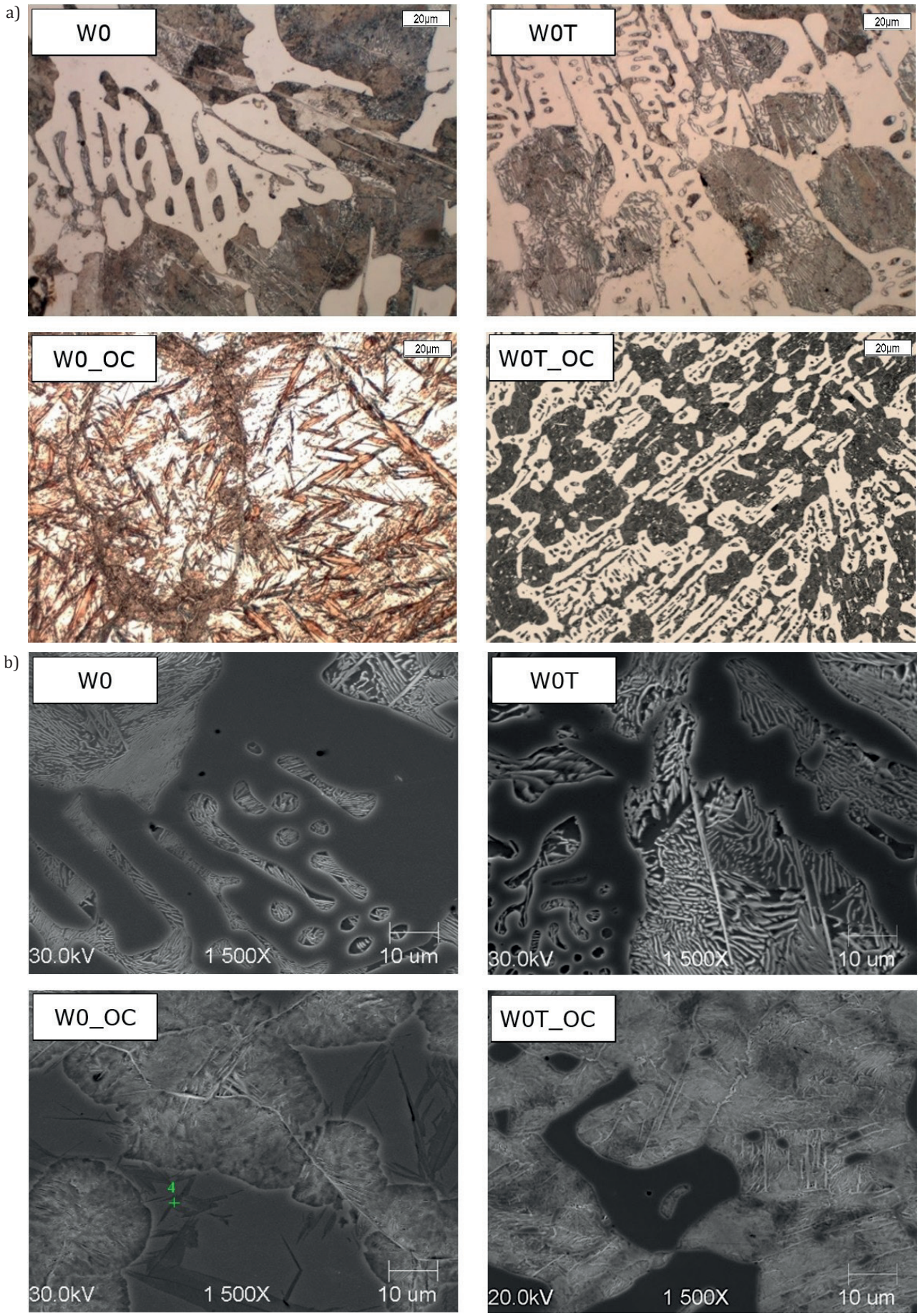

Fig. 3. Microstructures of samples W0, W0T, W0_OC and W0T_OC: a) optical micrographs (Nital etched, 500× magnification); b) scanning electron micrographs (SEM, 1500× magnification)

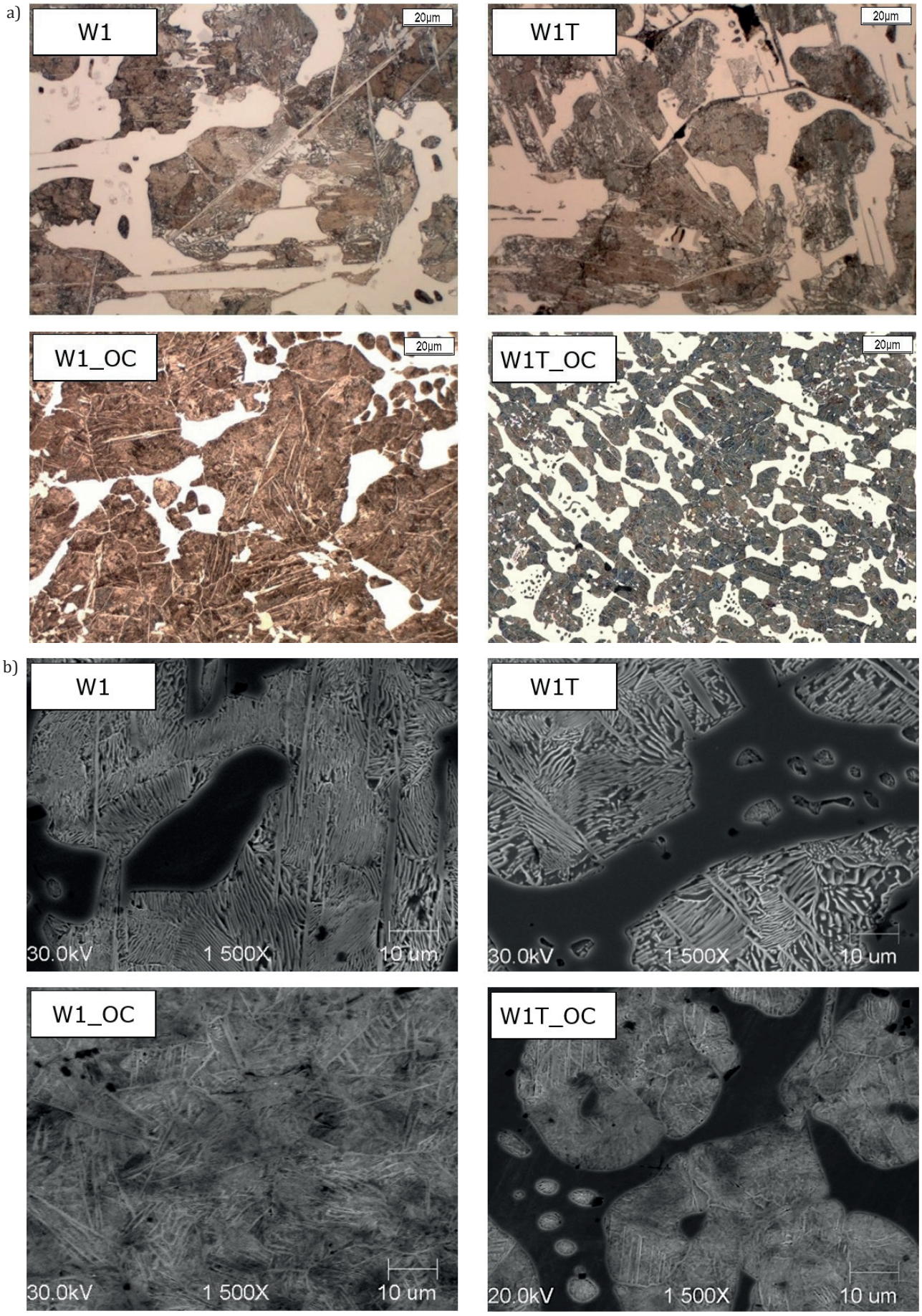

Fig. 4. Microstructures of W1, W1T, W1_OC and W1T_OC samples: a) optical micrographs (Nital etched, 500× magnification); b) scanning electron micrographs (SEM, 1500× magnification)

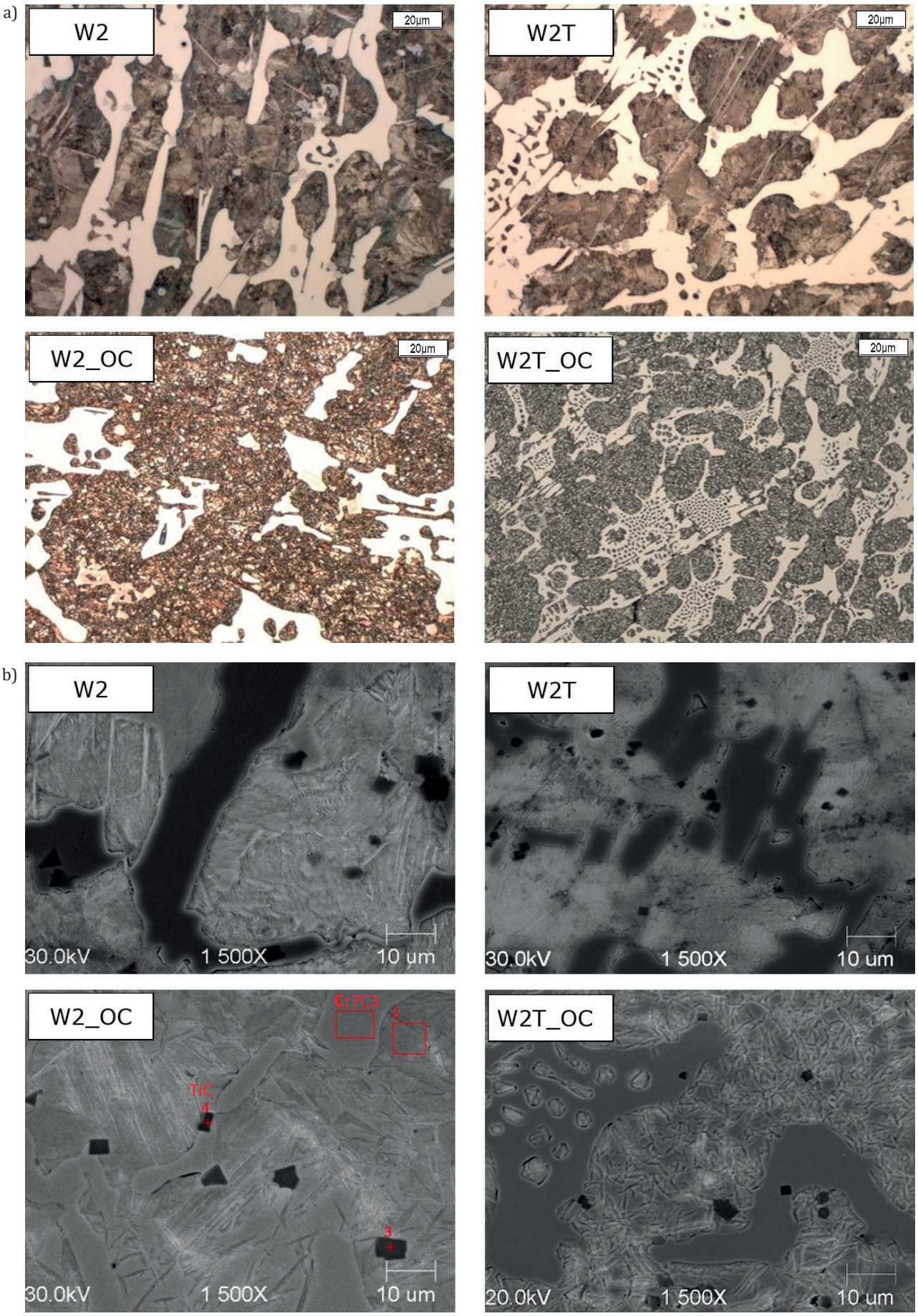

Fig. 5. Microstructures of W2, W2T, W2_OC and W2T_OC samples: a) optical micrographs (Nital etched, 500× magnification); b) scanning electron micrographs (SEM, 1500× magnification)

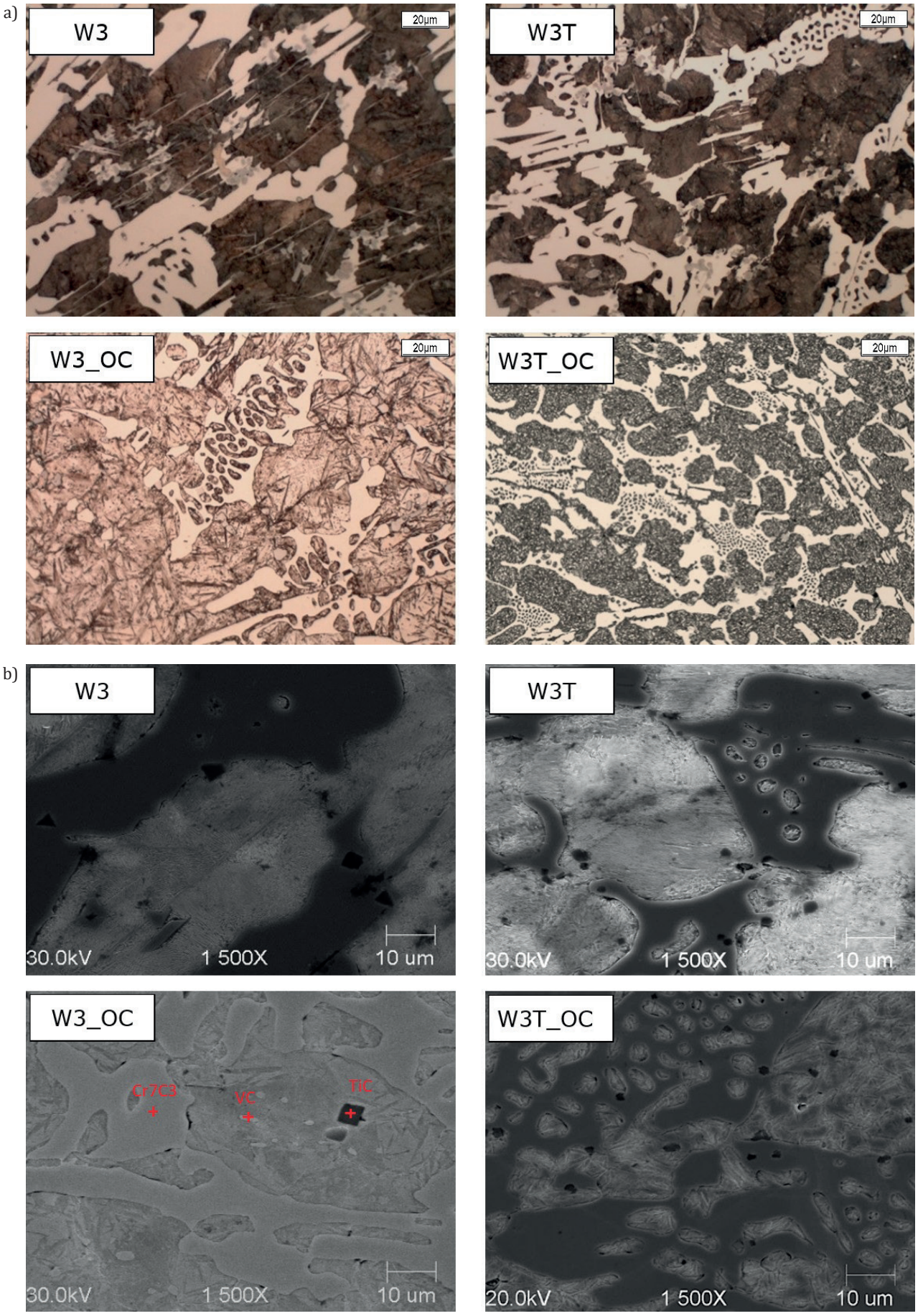

Fig. 6. Microstructures of W3, W3T, W3_OC and W3T_OC samples: a) optical micrographs (Nital etched, 500× magnification); b) scanning electron micrographs (SEM, 1500× magnification)

The application of heat treatment to all samples (W0_OC, W1_OC, W2_OC, W3_OC, W0T_OC, W1T_OC, W2T_OC, W3T_OC) consistently resulted in the refinement of cementite and improved regularity. In the combined samples (W0T_OC, W1T_OC, W2T_OC, W3T_OC), the synergy of tellurium and heat treatment produced the most favorable microstructures: highly fragmented cementite, a homogeneous matrix, and regular, fine inclusions of hard phases. Specifically, the W3T_OC sample, containing Ti, Cr, V, and Te after heat treatment, exhibited an optimal microstructural arrangement – very homogeneous, with a high content of dispersed hard phases within a fine-grained matrix.

In each analyzed sample, observations indicated that tellurium affected the morphology of cementite and carbides. Furthermore, it was evident that heat treatment led to their fragmentation and changes in the matrix structure. The combination of both methods resulted in the greatest fragmentation and ordering of the microstructure. In summary, the addition of tellurium acts as an effective modifier of the cementite and carbide microstructure, while heat treatment enables the further refinement and stabilization of the structure. The combination of both methods, particularly in the WxT_OC variants, significantly improved the microstructure of white cast iron, especially in alloys containing alloying additives (Ti, Cr, V).

The SDAS (Secondary Dendrite Arm Spacing) coefficient was determined at a magnification of 200×. As shown in Figure 7, the SDAS value consistently decreases with each new element introduced to the alloy when tellurium is also present. Without tellurium, the coefficient value does not show any easily identifiable trend. For samples W0 and W1 after heat treatment, no dendrites were observed, hence the SDAS coefficient could not be determined.

4. CONCLUSION

This study thoroughly investigated the influence of tellurium (Te) addition and heat treatment on the microstructure of hypoeutectic white cast iron, both in its as-cast state and with different alloying elements (titanium, chromium, and vanadium). The key findings are summarized below:

- The addition of tellurium significantly impacts the morphology of cementite and carbide phases across all analyzed samples. It consistently promotes their fragmentation and leads to a more uniform distribution throughout the microstructure.
- Heat treatment independently contributes to further fragmentation of these hard phases and induces beneficial changes in the matrix structure.
- The combination of tellurium addition and heat treatment proved to be the most effective strategy, resulting in the highest degree of microstructural homogeneity and fragmentation. This synergy led to highly refined microstructures with finely dispersed hard phases within a uniform matrix.
- For the baseline sample (W0), the combined effect of tellurium addition and heat treatment (W0T_OC) yielded the greatest microstructural homogeneity and stability. This was attributed to the inhibition of austenite-to-martensite transformation and enhanced carbide stabilization.
- A crucial observation was that tellurium stabilizes the formed carbides. In samples without tellurium, carbides showed signs of degradation during heat treatment, whereas in tellurium-containing samples, their structure remained intact, highlighting tellurium's protective role.

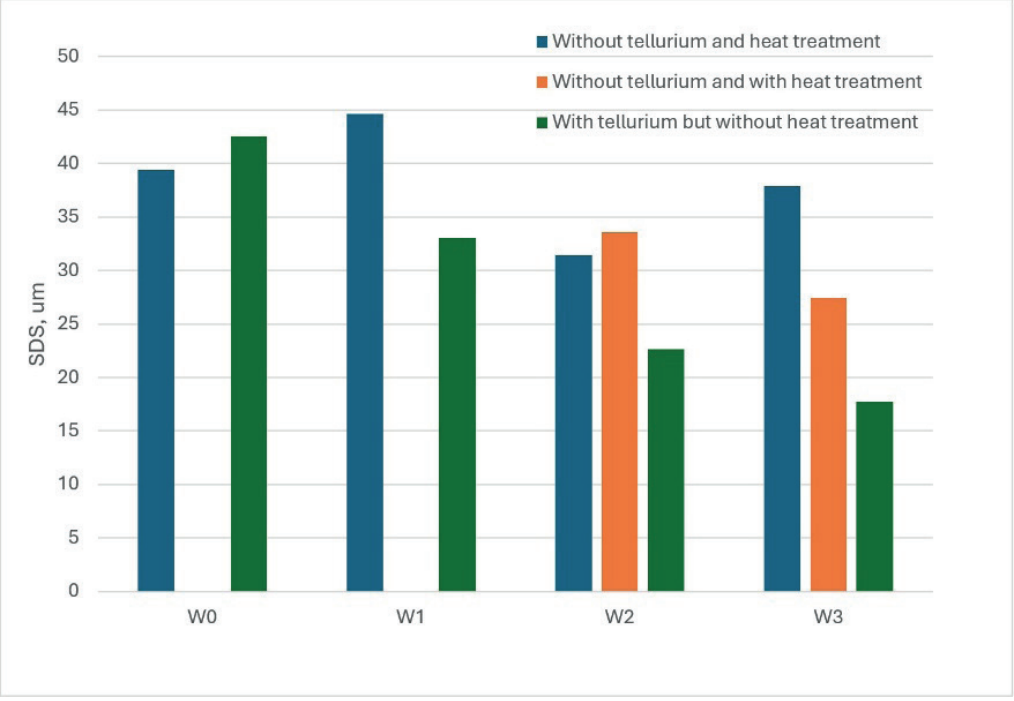

Fig. 7. Graph showing the results of determining the SDAS parameter for samples W0, W1, W2, W3, W0T, W1T, W2T, W3T, W0_OC, W1_OC, W2_OC, W3_OC

- Analysis of the Secondary Dendrite Arm Spacing (SDAS) parameter revealed that the presence of tellurium, particularly in combination with other alloying elements, leads to a significant reduction in the distance between dendrite arms. This suggests that tellurium intensifies the crystallization process, promoting a finer and more homogeneous casting structure.

In conclusion, tellurium acts as an effective modifier for the microstructure of cementite and carbides in hypoeutectic white cast iron. When combined with heat treatment, this approach offers a powerful method to achieve highly refined and stable microstructures, particularly beneficial in alloys containing titanium, chromium, and vanadium. These findings underscore the potential of tellurium as a critical alloying element for tailoring the properties of white cast iron for demanding applications.

ACKNOWLEDGMENTS

This research was conducted within Horizon Europe Project No. 101159771 – NetCastPL4.0.

REFERENCES

[1] Ueda S., Suzuki S., Yoshikawa T. & Morita K. (2017). Thermodynamic property of tellurium in molten iron measured by the transpiration method. *ISIJ International,* 57(3), 397–403. DOI: https://doi.org/10.2355/isijinternational.ISIJINT-2016-633.

[2] Alonso G., Stefanescu D.M., Bravo B., Aguado E. & Suarez R. (2022). Effect of tellurium on the nucleation process of spheroidal graphite in cast iron. *Journal of Materials Research and Technology,* 20, 1957–1968. DOI: https://doi.org/10.1016/j.jmrt.2022.07.004.

[3] Zheng L., Lou J., Yan B., B. Ren B., Li H. & Jiang Z. (2023). Effect of surfactant tellurium on the microstructure and mechanical properties of M42 high-speed steel. *ISIJ International*, 63(10) 1687–1696. DOI: https://doi.org/10.2355/isijinternational.ISIJINT-2022-504.

[4] Doğan N., Laird G.I. & Hawk J. (1995). Abrasion resistance of the columnar zone in high Cr white cast irons. *Wear*, 181–182, 342–349.

[5] Chung R.J., Tang X., Li D., Hinckley B. & Dolman K. (2009). Effects of titanium addition on microstructure and wear resistance of hypereutectic high chromium cast iron Fe-25wt.% Cr-4wt.%C. *Wear*, 267(1–4), 356–361. DOI: https://doi.org/10.1016/j.wear.2008.12.061.

[6] Radzikowska J.M. (2004). Metallography and Microstructures of Cast Iron. In: Vander Voort G.F. (Ed.), *ASM Handbook, Volume 9: Metallography and Microstructures*, 565–587. DOI: https://doi.org/10.31399/asm.hb.v09.a0003765.

[7] Heino V., Kallio M., Valtonen K. & Kuokkala V.T. (2017). The role of microstructure in high stress abrasion of white cast irons, *Wear,* 388–389, 119–125. DOI: https://doi.org/10.1016/j.wear.2017.04.029.

[8] Kopyciński D., Kawalec M., Szczęsny A., Gilewski R. & Piasny S. (2013). Analysis of the structure and abrasive wear resistance of white cast iron with precipitates of carbides. *Archives of Metallurgy and Materials*, 58(3), 973–976. DOI: https://doi.org/10.2478/amm-2013-0113.

[9] Shen P., Yang Q., Zhang D., Yang S. & Fu J. (2018). The effect of tellurium on the formation of MnTe-MnS composite inclusions in non-quenched and tempered steel. *Metals (Basel),* 8(8), 639. DOI: https://doi.org/10.3390/met8080639.

[10] Pokusová M., Berta I. & Murgašová M. (2018). Metallurgical processing of Al-Si alloys with increased iron content using sodium, strontium, and tellurium. *Journal of Casting & Materials Engineering*, 2(1), 9–13. DOI: https://doi.org/10.7494/jcme.2018.2.1.9.

[11] Nikolić F., Štajduhar I. & Čanađija M. (2021). Casting microstructure inspection using computer vision: Dendrite spacing in aluminum alloys, *Metals (Basel)*, 11(5), 756. DOI: https://doi.org/10.3390/met11050756.

[12] Kaya S., Yılan F. & Urtekin L. (2022). Influences of Cr on the microstructural, wear and mechanical performance of high-chromium white cast iron grinding balls, *Journal of Materials and Manufacturing*, 1, 23–30, 2022. DOI: https://doi.org/10.5281/zenodo.7107351.

Journal of Casting & Materials Engineering Vol. 9 No. 4 (2025) 59–65
https://doi.org/10.7494/jcme.2025.9.4.59

The Implementation Potential of the Hybrid Hot Metal Desulfurization Model – The Transformation of Research Results into Technological Recommendations

Angelika Podolska-Loska[1,2] *, Jan Falkus[1]

[1] AGH University of Krakow, Faculty of Metals Engineering and Industrial Computer Science, 66 Czarnowiejska St., Krakow, 30-059, Poland
[2] ArcelorMittal Poland S.A., 92 Piłsudskiego Ave., Dąbrowa Górnicza, 41-308, Poland
e-mail: podolska@agh.edu.pl

Received: 10 July 2025/Accepted: 11 November 2025/Published online: 23 December 2025.
This article is published with open access at AGH University of Science and Technology Journals.

Abstract

This study presents the development of a hybrid model for the desulfurization of hot metal using dual reagent injection of CaO and Mg, integrating thermodynamic equilibrium calculations with kinetic analysis based on Tank Theory. The objective is to provide practical technological recommendations that enable effective industrial application of the process. The model allows real-time simulation of sulfur concentration changes under varying parameters such as reagent dosage and mixing intensity, while an optimization module supports the selection of operating conditions by balancing desulfurization efficiency with material consumption and operational costs. The system adapts to changing technological conditions including feedstock composition and process temperature, ensuring flexibility in industrial practice. In addition to process control, the model incorporates economic evaluation by correlating reagent consumption with achieved technological outcomes, which enhances its practical value. The proposed solution represents a step toward intelligent desulfurization systems that combine the precision of physicochemical modeling with the adaptability of modern process control. Implementation of the hybrid model may lead to higher efficiency, reduced consumption of consumables, and stable achievement of target sulfur levels, thereby strengthening the economic competitiveness of iron production.

Keywords:

hot metal, desulfurization, hybrid, model, computer modeling

1. INTRODUCTION

Desulfurization remains a critical operation in iron and steelmaking, directly influencing the mechanical properties, weldability, and downstream process stability of final steel products. Sulfur, despite its low concentration, acts as a potent embrittling agent and must be removed efficiently at the earliest possible stage of production [1].

One promising approach is the desulfurization of hot metal using the dual reagent injection method of calcium oxide (CaO) and metallic magnesium (Mg), which leverages the simultaneous action of two complementary reagents with distinct thermodynamic properties. In this method, powdered CaO and Mg are introduced concurrently into the metal bath, typically using nitrogen as a carrier gas [2, 3]. A schematic diagram of the desulfurization station is presented in Figure 1. The reaction mechanism encompasses both heterogeneous reactions at the metal-slag interface and reactions within the bulk of the liquid metal, where gaseous Mg significantly enhances the diffusion of reactive species [4, 5].

A key advantage of the dual reagent injection method is the synergistic behavior of its components: magnesium initiates the process rapidly through an exothermic surface reaction ($Mg + S \rightarrow MgS$), while calcium oxide ensures deep desulfurization due to its high sulfur capacity under low oxygen activity [6, 4]. Both laboratory and industrial studies confirm that this synergy enables desulfurization degrees of up to 95%, while simultaneously reducing operational costs by 10–20% compared to single-agent desulfurizers [3].

To contextualize the proposed method, it is useful to contrast it with desulfurization techniques applied at later stages of steelmaking. In secondary metallurgy, calcium cored wire (CaSi) injection is commonly used to refine molten steel, improving cleanliness and mechanical performance. However, such techniques are not directly applicable to hot metal due to differences in temperature, slag composition, and oxygen activity [7]. CaSi wire is typically introduced under controlled ladle furnace conditions, whereas the CaO+Mg dual reagent injection method targets hot metal prior to converter processing.

The proposed technique is suitable for iron alloys intended for the production of low-sulfur carbon steels and low-alloy steels, where the sulfur content must be reduced below 0.005% to meet mechanical and weldability requirements. Early-stage desulfurization of hot metal not only improves downstream process stability but also reduces the burden on secondary refining operations.

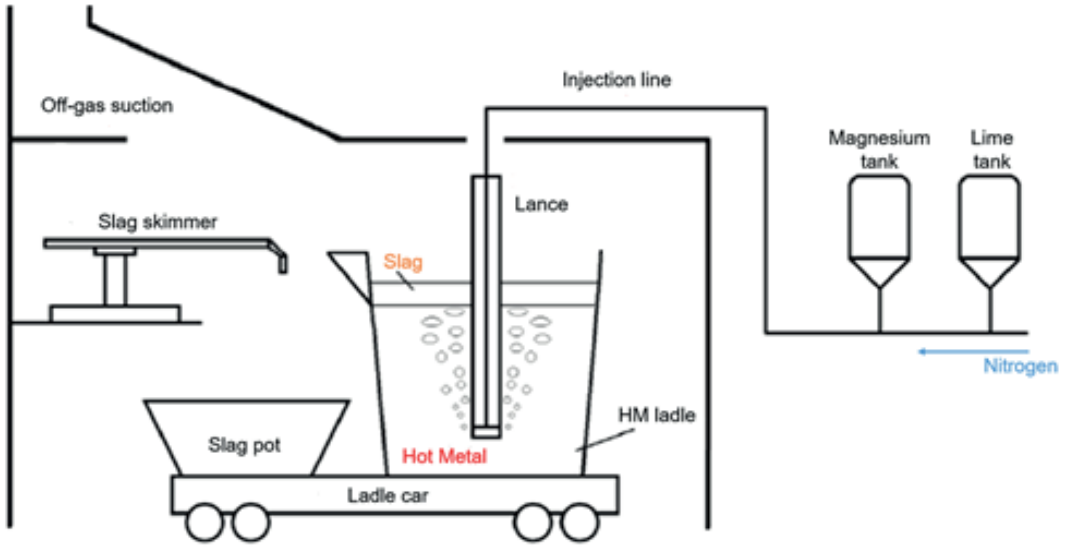

Fig. 1. Schematic diagram of the hot metal desulfurization station using the dual reagent injection method CaO+Mg [10]

The aim of this study is to evaluate the implementation potential of a hybrid model for hot metal desulfurization using CaO and Mg dual reagent injection, integrating thermodynamic equilibrium calculations and kinetic mixing analysis [8]. The model is designed to support technological decision-making under industrial conditions, enabling process optimization in terms of reagent consumption, sulfur removal efficiency, and economic performance [9].

2. RESEARCH METHODOLOGY

The initial task undertaken involved the identification of both control parameters and state parameters for the hot metal desulfurization process (Table 1). The objective of this step was to determine those factors for which modification would be feasible. It should be noted that both control and state parameters can be classified into two overarching categories: thermodynamics and kinetics parameters.

Table 1
Set of parameters for the hot metal desulfurization process: green colour represents control parameters, blue colour represents state parameters

Thermodynamics	Kinetics
Hot metal analysis (C, Si, Mn, P, S)	Average material flow during the process
Hot metal mass	Material injection time
Hot metal temperature	Pressure in material tanks
Final sulfur content (desulfurization level)	Transport gas pressure
Slag mass	Carrier gas flow
Injected material mass	
Initial material mass in the tanks	

The next stage of the research involved conducting simulations of the desulfurization process using historical data obtained from an actual metallurgical unit. The baseline (initial) values used in the simulation model reflect the process conditions of real industrial heat, which served as the reference case for all parameter variations. A complete set of these baseline parameters is presented in Table 2. To accurately assess the real impact of individual factors on the simulated sulfur content after the desulfurization process, a decision was made to change only one parameter at a time.

Table 2
Baseline process parameters used in the simulation model

Parameter	Value	Unit
Temperature	1391	°C
Hot metal mass	293	Mg
Sulfur initial	0.031	%
Mg mass injected	0.099	Mg
CaO mass injected	0.523	Mg
Slag mass	4	Mg

In the Tank Theory model, mass transfer streams between the elementary reactors were introduced to reflect the intensity of mixing and reagent dispersion within the ladle. These mass transfer values are directly linked to the nitrogen flow rate used in the industrial process, which governs the dynamic exchange of material between reactive zones. By adjusting these values, the simulation captures the influence of flow-induced mixing on desulfurization efficiency. A simplified schematic of the model operation is presented in Figure 2.

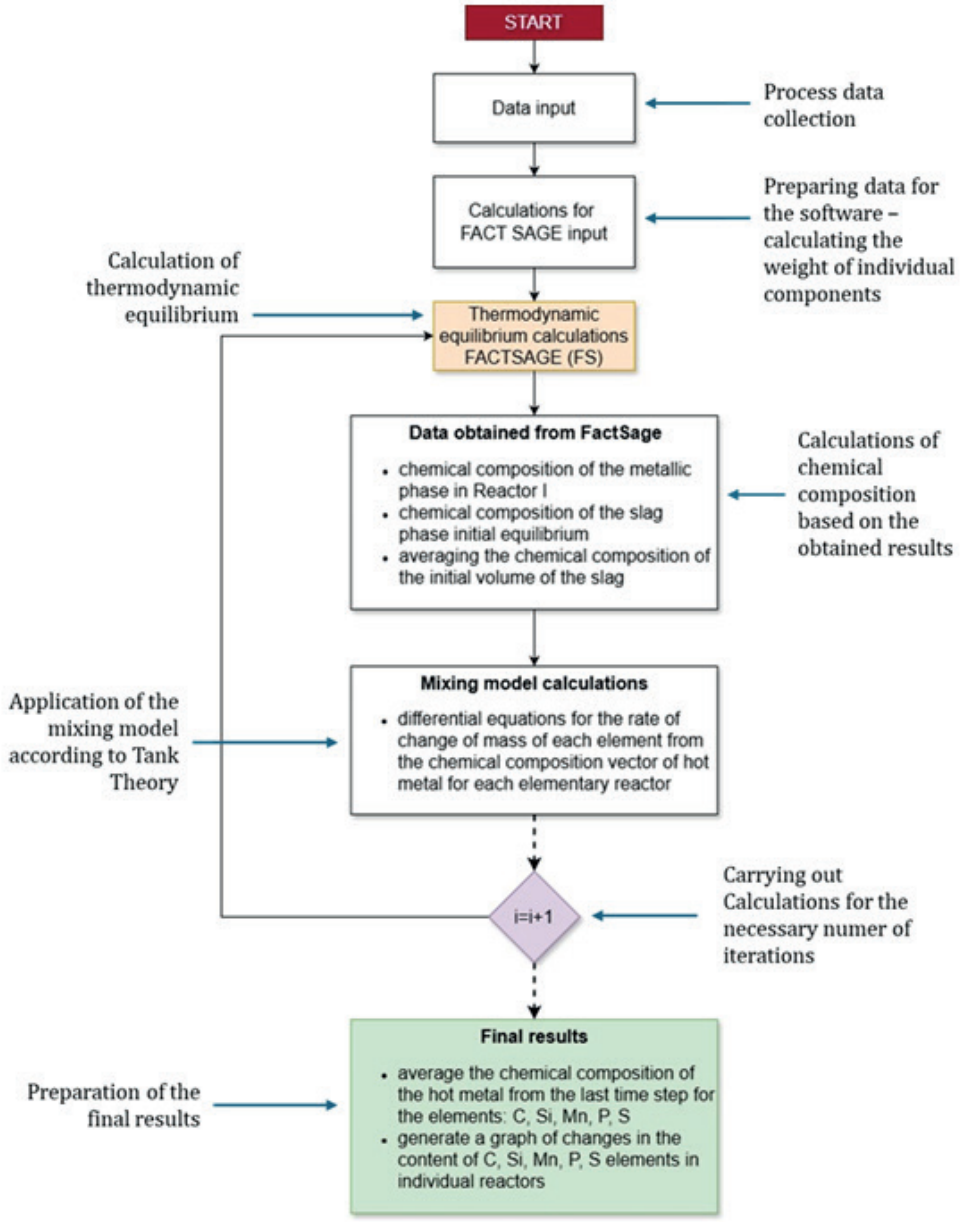

Fig. 2. Simplified block diagram of the hybrid hot metal desulfurization model

3. ANALYSIS AND DISCUSSION OF THE OBTAINED RESULTS

Simulations of the desulfurization model were conducted by varying the following parameters: the mass of blast furnace slag in the ladle, the amount of CaO introduced into the process, the amount of Mg introduced into the process, the temperature of the hot metal, the exchange of sizes between elementary reactors 1 and 3, as well as changes in the mass transfer rates between the elementary reactors. The sulfur content after the process, as a function of each investigated parameter, is presented in Figures 3–7.

To represent the mixing and reaction behavior within the hot metal bath, the system was conceptually divided into three elementary reactors arranged in series, following the Tank Theory model. Each reactor corresponds to a distinct zone of the ladle with different mixing intensities and reaction characteristics. Reactor 1 represents the surface region, where magnesium vapor reacts rapidly with sulfur at the metal-slag interface. Reactor 2 models the intermediate zone, characterized by partial mixing and reagent dispersion. Reactor 3 reflects the deeper region of the bath, where calcium oxide dissolves and reacts under low oxygen activity, enabling deep desulfurization. The exchange of sizes between reactors 1 and 3 simulates variations in the effective volume of reactive zones, while changes in mass transfer rates reflect differences in mixing efficiency and reagent penetration. This reactor-based approach allows the model to capture both thermodynamic equilibrium and kinetic limitations of the desulfurization process [2].

Figure 3 illustrates the variation in the mass of blast furnace slag in the ladle. Simulations were conducted for the baseline heat as well as for two modified values: a reduction of 50% and an increase of 50% relative to the baseline slag mass. The simulation results indicate that changes in the mass of blast furnace slag affect the final outcome of the desulfurization process. Specifically, a lower slag mass leads to a reduced sulfur content after the process.

Figure 4 illustrates the variation in final sulfur content as a function of the amount of CaO added to the process. The simulation was performed for the baseline heat and four modified values of CaO consumption: −40% of the baseline CaO mass, −20% of the baseline CaO mass, +20% of the baseline CaO mass, and +40% of the baseline CaO mass. The simulation results indicate that increasing the addition of CaO to the desulfurization process leads to a lower final sulfur content, thereby enhancing the degree of desulfurization [11].

Figure 5 illustrates the variation in final sulfur content as a function of the amount of Mg added to the process. The simulation was conducted for the baseline heat and four modified values of Mg consumption: −40% of the baseline Mg mass, −20% of the baseline Mg mass, +20% of the baseline Mg mass, and +40% of the baseline Mg mass. The simulation results indicate that increasing the addition of Mg to the desulfurization process leads to a lower final sulfur content, thereby enhancing the degree of desulfurization.

Figure 6 illustrates the effect of varying the hot metal temperature on the sulfur content after the desulfurization process. The temperature range investigated was 1315°C to 1420°C. Based on the conducted simulations, it can be concluded that lower hot metal temperatures result in more efficient utilization of Mg, ultimately leading to a lower final sulfur content [12].

Figure 7 illustrates the impact of two key modifications applied to the simulation model: the exchange of sizes between elementary reactors 1 and 3, and a 100% increase in mass transfer rates between the reactors. These changes were analyzed in four distinct configurations, combining baseline and modified reactor geometries with baseline and modified stream parameters. A detailed representation of these simulation variants is provided in Table 3.

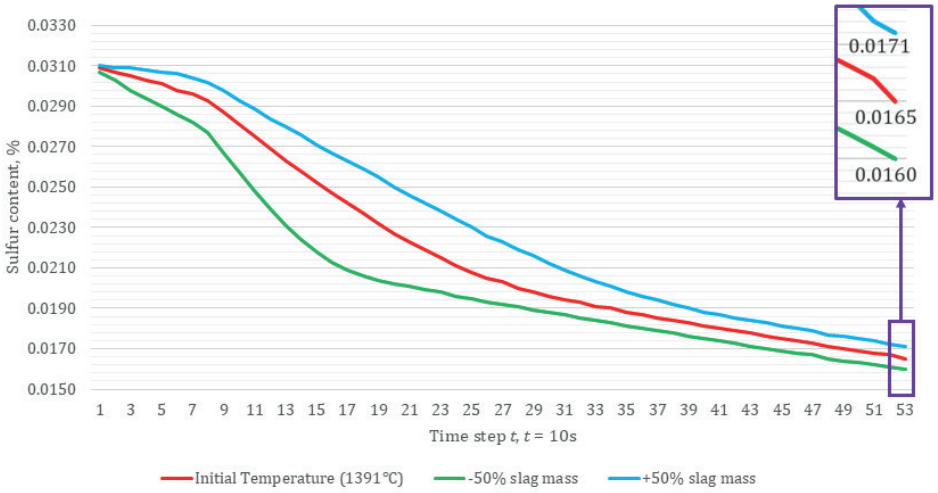

Fig. 3. Sulfur content depending on blast furnace slag mass

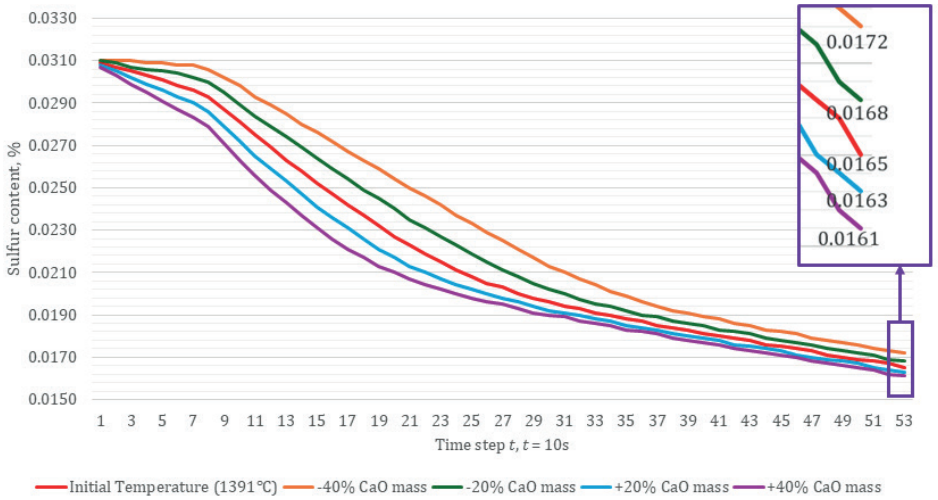

Fig. 4. Sulfur content depending on CaO addition

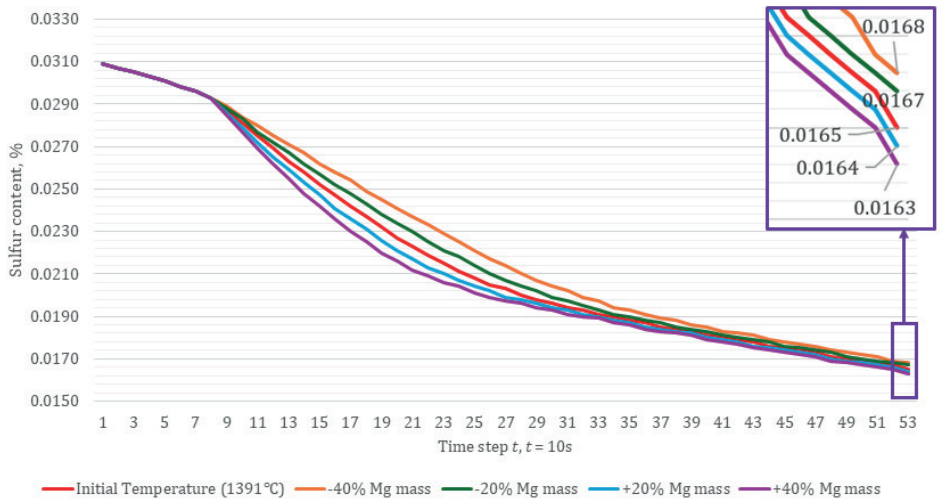

Fig. 5. Sulfur content depending on Mg addition

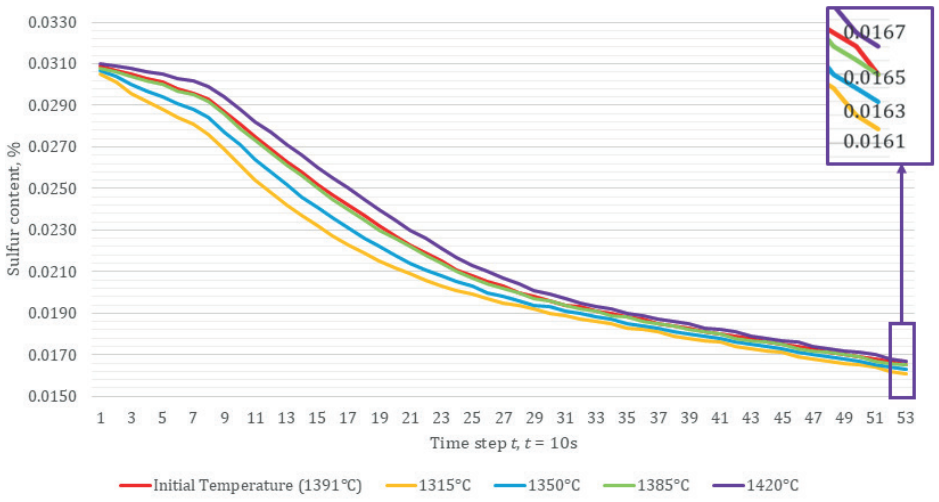

Fig. 6. Sulfur content depending on the HM temperature

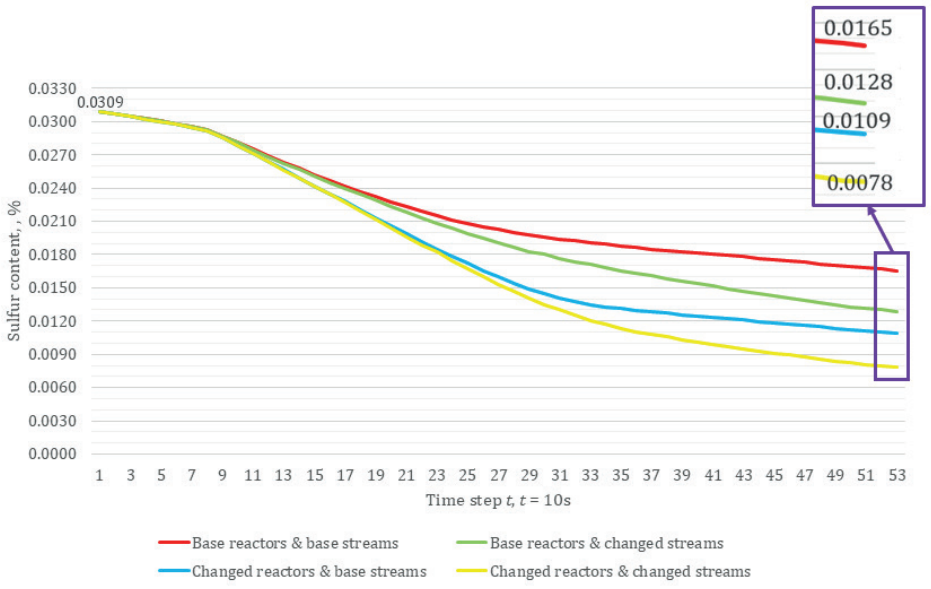

Fig. 7. Sulfur content depending on the parameter set

The results show that modifying the size of the elementary reactors leads to a lower degree of desulfurization for the same amount of reagents. This effect is attributed to the increased volume of reactor 1, which results in the delivery of a greater amount of sulfur to the chemical reaction zone. A similar trend is observed when the mass transfer rates between reactors are increased, indicating enhanced transport of sulfur to reactor 1. However, in this case, the effect also reflects intensified mixing within the ladle, which contributes to the overall reaction dynamics.

The configuration combining both modified reactor geometry and modified stream parameters yields the lowest final sulfur content (0.0078%), confirming that simultaneous optimization of spatial distribution and mass transfer enhances desulfurization efficiency.

Table 3
Simulation variants with reactor volumes and mass transfer stream values

Variant	Reactors volume	Mass transfer streams values
Based reactors & based streams	V_1 = 30% V_2 = 50% V_3 = 20%	V_{1-2} = 3% V_{1-3} = 2% V_{2-3} = 2.5%
Based reactors & changed streams	V_1 = 30% V_2 = 50% V_3 = 20%	V_{1-2} = 6% V_{1-3} = 4% V_{2-3} = 5%
Changed reactors & based streams	V_1 = 50% V_2 = 30% V_3 = 20%	V_{1-2} = 3% V_{1-3} = 2% V_{2-3} = 2.5%
Changed reactors & changed streams	V_1 = 50% V_2 = 30% V_3 = 20%	V_{1-2} = 6% V_{1-3} = 4% V_{2-3} = 5%

4. CONCLUSIONS AND SUMMARY

The experimental verification of the hybrid hot metal desulfurization model demonstrated significant implementation potential. Considering the catalytic effect of sulfur on the degradation of steel's mechanical properties, as well as its limited reactivity in subsequent stages of steelmaking (converter process, secondary metallurgy), the optimization of desulfurization parameters at the hot metal preparation stage remains a critical metallurgical challenge [13]. Industrial data confirm that early removal of sulfur enables its content to be reduced to below 0.005% by mass while maintaining process profitability. Based on the conducted simulations, the following conclusions were formulated:

- Both magnesium and calcium oxide play a thermodynamic role in the desulfurization process. The effectiveness of magnesium, in particular, is influenced by the mass and basicity of the blast furnace slag, which affect the stability of the MgS phase and the extent of sulfur removal.
- The most effective configuration combined modified reactor geometry with increased nitrogen flow, yielding the lowest final sulfur content (0.0078%). This confirms that the simultaneous optimization of spatial distribution and kinetic mixing parameters significantly improves desulfurization performance.
- Simulation results indicate that increasing CaO addition leads to a greater reduction in final sulfur content than increasing Mg addition under the tested conditions, highlighting the strong thermodynamic driving force associated with CaO-based desulfurization. Hot metal temperature affects the desulfurization process — lower temperatures enhance the efficiency of sulfur removal by promoting favorable thermodynamic conditions and increasing the stability of sulfide phases. The kinetic factor contributing to the increased efficiency of the desulfurization process is the nitrogen flow rate, which governs the intensity of mass transfer between the elementary reactors. Higher nitrogen flow enhances mixing and accelerates the transport of sulfur to the reaction zone, thereby improving the overall desulfurization performance. Figures 3–7 reveal that desulfurization kinetics are significantly influenced by both thermodynamic and kinetic parameters. Variations in slag mass, reagent dosing (CaO and Mg), initial temperature, and reactor-stream configurations modify the rate and extent of sulfur removal over time. These changes are reflected in the slope and curvature of the sulfur reduction curves, confirming that process dynamics must be considered alongside equilibrium conditions.

Not all of the process parameters influencing desulfurization efficiency can be directly translated into technological control algorithms. A notable example is the temperature of the metal bath, which exhibits a contradictory impact on process indicators. Lowering the temperature to the range of 1350–1400°C increases the efficiency of desulfurizing agents by improving the thermodynamic affinity of the reactions. However, this adjustment simultaneously necessitates an increase in the specific consumption of hot metal in the oxygen converter to compensate for energy losses.

Figure 8 presents a structured set of recommendations for the implementation of process improvements based on the simulation results. The proposed actions are categorized into two groups: those requiring no financial investment and those that involve additional costs.

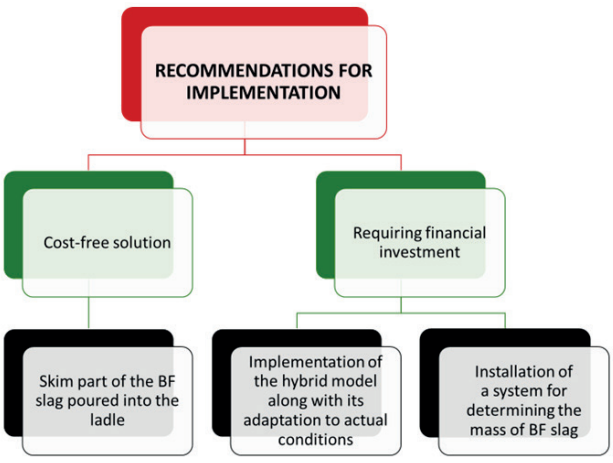

Fig. 8. Proposed recommendations

The cost-free recommendation involves partial skimming of the blast furnace slag poured into the ladle. This action aims to reduce the slag mass, which, as demonstrated in the simulations, can improve desulfurization efficiency by minimizing the dilution and buffering effects of the slag phase.

Recommendations requiring financial investment include the implementation of the hybrid simulation model adapted to actual operating conditions, and the installation of a system for determining the mass of blast furnace slag introduced into the ladle. These measures are intended to enhance process control and enable more precise reagent dosing, thereby improving the overall effectiveness of desulfurization [14].

The categorization of these recommendations reflects both the technical feasibility and economic consideration associated with their implementation.

ACKNOWLEDGEMENTS

The authors would like to thank the ArcelorMittal Poland S.A. for sharing the technical data which enabled the research to be conducted. This research was carried out as part of the Implementation Doctorate Program financed by the Ministry of Science and Higher Education due the contract no. DWD/5/0190/2021 of 29.12.2021.

REFERENCES

[1] van Hattum G., Schrama F. & van den Berg B. (2015). The leading hot metal desulfurization methods: A comparison between KR, MMI and CO-injection. In: *Proceedings of the Seminar on Steelmaking, Casting and Non-Ferrous Metallurgy ABM Week 2015. 46th International Steelmaking Seminar*, 46(46), pp. 323–332. DOI: https://doi.org/10.5151/1982-9345-26624.

[2] Podolska A. & Falkus J. (2023). Hot metal desulfurization process as an object of physical and mathematical modelling. In: *Proceedings 32nd International Conference on Metallurgy and Materials,* May 17–19, 2023, Brno, Czech Republic, pp. 13–19. DOI: https://doi.org/10.37904/metal.2023.4630.

[3] Ma W., Li H., Cui Y., Chen B., Liu G. & Ji J. (2017). Optimization of desulphurization process using lance injection in molten iron. *ISIJ International*, 57(2), 214–219. https://doi.org/10.2355/isijinternational.ISIJINT-2016-167.

[4] Lindstrom D. (2014). *A Study on Desulfurization of Hot Metal Using Different Agents* [doctoral dissertation]. Swedish KTH School of Industrial Engineering and Management.

[5] Łędzki A., Klimczyk A., Stachura R., Bernasowski M. & Migas P. (n.d.). *Technologia i podstawy sterowania procesami redukcji.* URL: https://home.agh.edu.pl/~zmsz/pl/pliki/Technologia_i_Podstawy_Sterowania_Procesami_Redukcji.pdf [11.06.2025].

[6] Lis T. (1995). Odsiarczanie stali wapniem i magnezem z udziałem tlenkowej fazy dyspersyjej. *Zeszyty Naukowe Politechniki Śląskiej. Hutnictwo,* 49.

[7] Buľko B., Molnár M., Demeter P., Červenka M., Tréfa G., Mochnacká M., Baricová D., Hubatka S., Fogaraš L., & Šabík V. (2022)., Deep steel desulfurization practice *Transactions of the Indian Institute of Metals*, 75, 2807–2816. URL: https://link.springer.com/article/10.1007/s12666-022-02643-0.

[8] Falkus J. (1998). *Fizyczne i matematyczne modelowanie procesów mieszania kąpieli metalowej w reaktorach metalurgicznych*. Kraków: AGH Uczelniane Wydawnictwa Naukowo-Dydaktyczne.

[9] Visser H.-J. & Boom R. (2006). Advanced process modelling of hot metal desulphurisation by injection of Mg and CaO. *ISIJ International*, 46(12), 1771–1778. DOI: https://doi.org/10.2355/isijinternational.46.1771.

[10] Biljan S.N. (2014). Problems and approaches for solutions in modern injection technologies. In: *13th International Symposium for Desulfurization of Hot Metal and Steel*, Almamet GmbH, 1–4 October 2014, Montecatini Terme, Italy, 51–55.

[11] Shen J.-M., Lin C.-M., Chang Y.-E., Lin H.-J. & Wu W. (2024). Effects of different CaO/Al_2O_3 ratios on the phase composition and desulfurization ability of CaO-based desulfurizers in hot metal. *Metals*, 14(3), 363. DOI: https://doi.org/10.3390/met14030363.

[12] Li M., Peng J., Li S., Chen R., Li C., Bao G. & Lv S. (2025). Reaction kinetics of desulphurisation of hot metal using $CaO–SiO_2–Al_2O_3–MgO–TiO_2–Na_2O$ slag systems. *Ironmaking & Steelmaking*, 52(7). DOI: https://doi.org/10.1177/03019233251313935.

[13] Schrama F. (2021). Desulphurisation in 21st century iron- and steelmaking (Doctoral dissertation). Delft University of Technology, Delft, Netherlands. https://doi.org/10.4233/uuid:4f1e8ff6-e910-4048-8a17-2a959c74f508.

[14] Piva S.P.T. & Pistorius P.C. (2021). Data-driven study of desulfurization during ladle treatment and its impact on steel cleanliness. In: *2021 AISTech Conference Proceedings*. Nashville, TN, USA. DOI: https://doi.org/10.33313/382/085.

Journal of Casting & Materials Engineering Vol. 9 No. 4 (2025) 66–71
https://doi.org/10.7494/jcme.2025.9.4.66

The Influence of the Knock-out Additive on the Mechanical Properties of Cores Made in the Core Blowing Process

Artur Bobrowski[1,*], Jakub Kowalski[1]

[1] AGH University of Krakow, Faculty of Foundry Engineering, 23 Reymonta St., 30-059 Krakow, Poland
**e-mail:arturb@agh.edu.pl.pl*

Received: 28 October 2025/Accepted: 28 November 2025/Published online: 23 December 2025.
This article is published with open access at AGH University of Science and Technology Journals.

Abstract

The article presents the results of research on the effect of an additive improving shakeout (perlite ore with a specified grain size) on the mechanical properties of cores produced by the blowing process. The study was conducted on cores (standard specimens for tensile strength testing) made from core sands with varying amounts of loosening additive, depending on the core box temperature and shooting time, at a constant operating pressure of the shooting machine. The temperature of the core box at which the cores achieved the best mechanical properties was identified, and the necessity of optimizing both the amount of perlite ore additive and the binder content in the core sand to ensure the required mechanical properties of the cores was demonstrated.

Keywords:

foundry, core sand, blowing process, inorganic binder, knocking-out, perlite ore

1. INTRODUCTION

Sand cores are a key component of a casting mold, and their purpose is to reproduce the internal shapes of the casting with a surface that is as smooth and defect-free as possible. In foundry practice, single-use sand cores are most commonly used, and they must meet numerous requirements, including technological and mechanical ones [1]. Good cores should provide adequate initial mechanical strength to allow safe removal from the core box. They should maintain the required strength during storage before being placed in the mold cavity just prior to pouring, as well as during assembly in the mold cavity itself. However, the core-making process using blowing methods has two main disadvantages: a higher degree of compaction along the axis of the core vents and binder migration under the influence of the air stream [2].

Another important technological feature that high-quality cores should possess is resistance to thermal deformation. To reduce the roughness of the internal surface of the casting, cores are usually made from fine-grained base sands. Cores are exposed to the extreme conditions prevailing inside the mold cavity and are often completely burned out during casting. If organic binders are used, no technological problems arise during the removal of the core from the finished casting. In contrast, when inorganic binders (e.g. water glass or other silicate binders) are employed, problems with shakeout occur. Under the influence of the high temperature of the molten metal, so-called secondary hardening takes place in silicate binders, accompanied by a rapid increase in strength – referred to as final strength [3, 4]. This hardening effect causes technological difficulties associated with removing the core from the casting or the entire mold. Poor shakeout leads to additional production costs due to increased labor and energy consumption, reduced efficiency, and sometimes the need to remake the casting. Many attempts have been made to improve the shakeout properties of molding and core sands by modifying the binder itself or by introducing additives into the sand mixture to reduce final strength, thereby improving shakeout.

Inorganic binders are among the most environmentally friendly, as they do not emit harmful decomposition products during mold pouring [5, 6] and can be hardened by both physical and chemical methods [4, 7–13]. When selecting additives for molding and core sands, both technological and environmental aspects must be considered.

The search for a loosening additive that improves shakeout while also meeting environmental requirements led to the selection of perlite ore as an inorganic material characterized by its volume change under the influence of temperature [14–17], which consequently disrupts the continuity of the hardened binder, reducing final strength and enhancing shakeout [18]. As an inorganic material, it does not emit harmful chemical compounds. The aim of this study was to determine the effect of the selected perlite ore on the mechanical properties (bending strength) of foundry cores

produced using the warm-box technology with the inorganic binder Cordis [19]. The work includes a detailed analysis of changes in core strength depending on the amount of loosening additive and the varying parameters of the blowing process. The optimal parameters of the core production process using a core shooting machine were determined. Previously published studies in this area covered research on mechanical and technological properties of cores (standard specimens) produced by vibration compaction [18, 20, 21], made with the inorganic binder Geopol [4, 22].

2. METHODOLOGY

For core production, a LUT-type core shooter manufactured by Multiserw-Morek (Fig. 1) [23] was used. This device allows for the adjustment of blowing process parameters such as shooting pressure, shooting time, heating temperature, and heating time.

a)

b)

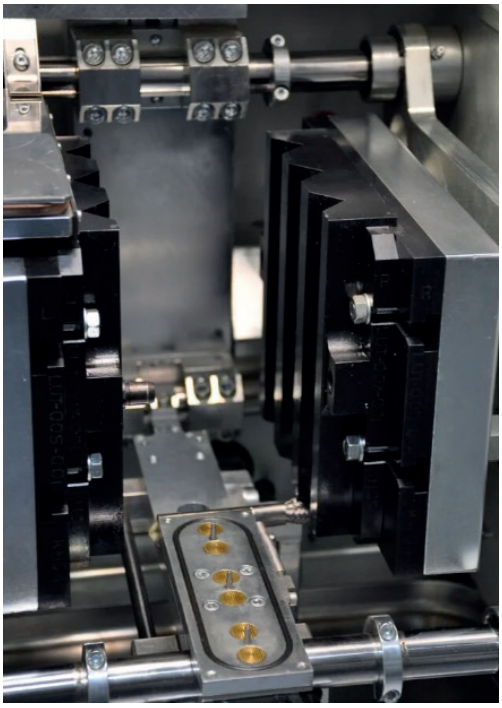

Fig. 1. Universal machine for making test samples and small cores (a) and core box for making standard bending samples (b) [23]

The core sands were prepared using quartz sand BK 5.0D from the "Szczakowa" mine, owned by DBCargo [24]. The perlite ore originated from a Slovak deposit. Sieve analysis was performed on a standard set with mesh sizes ranging from 0.056 to 1.6 mm (average of two measurements), in accordance with the Polish Standard PN–85/H–11001 [25]. The analysis was carried out twice for each material on 50 g samples, and the results are presented in Tables 1 and 2.

Table 1
Sieve analysis of quartz sand

Sieve number	Residue on sieves [%]		Characteristic indicators of the tested quartz sands
	Sample 1	Sample 2	
1.600	0.00	0.00	Number of grains, AFS = 56.10
0.800	0.02	0.00	Average grain size = 0.23 mm
0.630	0.07	0.06	Geometric average = 0.25 mm
0.400	1.76	1.76	Arithmetic average = 0.26 mm
0.320	6.51	6.62	Harmonic average = 0.26
0.200	30.11	30.06	Median = 0.25
0.160	6.82	7.13	Average grain size = 0.25
0.100	4.55	4.23	Main fraction = 87.25%
0.071	0.15	0.13	Separation factor = 1.22
0.056	0.01	0.01	Inclination indicator = 0.96
Bottom	0.00	0.00	Degree of homogeneity = 75%
Total	50.00	50.00	Surface area = 9.59 m^2/kg

Table 2
Sieve analysis of perlite ore

Sieve number	Residue on sieves [%]		Characteristic indicators of the tested perlite ore
	Sample 1	Sample 2	
1.600	0.00	0.00	Number of grains, AFS = 52.27
0.800	0.00	0.00	Average grain size = 0.24 mm
0.630	0.84	1.00	Geometric average = 0.31 mm
0.400	15.10	14.98	Arithmetic average = 0.34 mm
0.320	10.85	9.77	Harmonic average = 0.26
0.200	13.09	16.00	Median = 0.33
0.160	4.28	3.65	Average grain size = 0.33
0.100	4.15	3.21	Main fraction = 79.79%
0.071	0.71	0.51	Separation factor = 1.38
0.056	0.26	0.27	Inclination indicator = 0.93
Bottom	0.72	0.61	Degree of homogeneity = 50%
Total	50.00	50.00	Surface area = 8.79 m^2/kg

The core sands were prepared with a constant binder content – 2.5 parts by weight of binder per 100 parts by weight of the sand base. As the binder, the inorganic Cordis binder from Hüttenes-Albertus [19] was used. The first prepared core sand mixture, which did not contain the loosening additive (perlite ore), was treated as the reference mixture. The other two core sand mixtures contained the loosening additive – perlite ore. The composition of the core sand mixtures used in the study is presented in Table 3.

Table 3
Composition of core sands M0, M4 and M8

Core sand	Component of the core sand, in parts of mass		
	Quartz sand	Binder	Perlite ore
M0	100	2.5	0.0
M4	100	2.5	4.0
M8	100	2.5	8.0

All core sand mixtures were prepared using a rotor mixer, with a mixing time of 1 minute. The prepared standard specimens (cores) for determining bending strength were set aside for 1 hour to cool and properly harden. The bending strength tests were carried out using an LRu-2e testing device manufactured by Multiserw-Morek (Fig. 2) [26].

Standard specimens for bending strength testing were produced each time at an operating pressure of 5 bar, but with two different shooting times (0.8 and 1.2 s) and three temperature levels: 140, 160, and 180°C. The holding (curing) time of the samples in the core box was constant and amounted to 120 s. The results presented in the article represent the arithmetic mean of three measurements.

Fig. 2. LRu-2e device for testing the strength of molding and core sands [26]

3. RESULTS

Figure 3 presents the bending strength results for the reference core sand mixture – without the loosening additive (perlite ore) – as a function of the core box temperature, for two shooting times: 0.8 and 1.2 s.

From Figure 3, it follows that for the mixture without the addition of perlite ore, the highest bending strength (3.58 MPa) was obtained at a core box temperature of 140°C and a shooting time of 1.2 s. Increasing the core box temperature resulted in lower strength values, namely 2.89 MPa at 160°C and 3.32 MPa. The obtained results also indicate that shortening or extending the shooting time of the core sand into the core box is not particularly significant, as the bending strength values obtained are very similar, and the differences are mainly due to statistical error.

The introduction of 4.0 parts by mass of perlite ore into the core mixture while maintaining the binder content at 2.5 parts by mass relative to the base material resulted in a decrease in bending strength by approximately 1.0 MPa (Fig. 4). This significant, about 20%, reduction in strength should be attributed to the introduction of an additional component, which increased the specific surface area that needed to be coated with the binder layer. The higher number of individual grains requiring binder coverage means that, in quantitative terms, there is less binder available relative to the total amount of grains – quartz sand and perlite ore. It should also be noted that the loosening additive (perlite ore) contains approximately 2% of particles smaller than 0.1 mm (Table 2), which further intensifies the increased binder demand.

It was also observed that for this core mixture, the best mechanical properties were obtained at a core box temperature of 180°C. The lower strength values obtained with a longer shooting time result from the reduced flow rate from the shooting chamber of the core shooter, which may lead to a lower degree of compaction of the core mixture in the core box – particularly in the case of core mixtures with lower flowability.

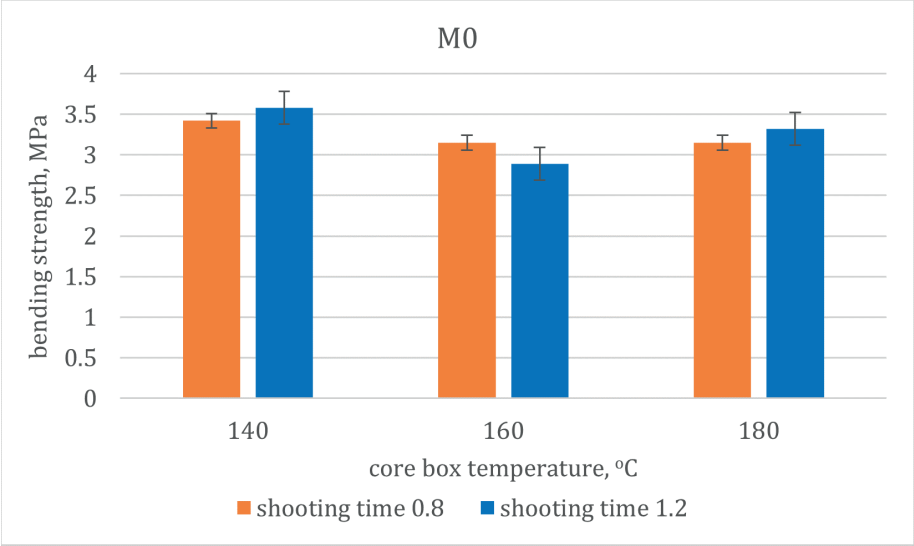

Fig. 3. The bending strength of standard specimens made from the reference core sand mixture (without the addition of perlite ore, M0) as a function of the core box temperature and shooting time for the mixture

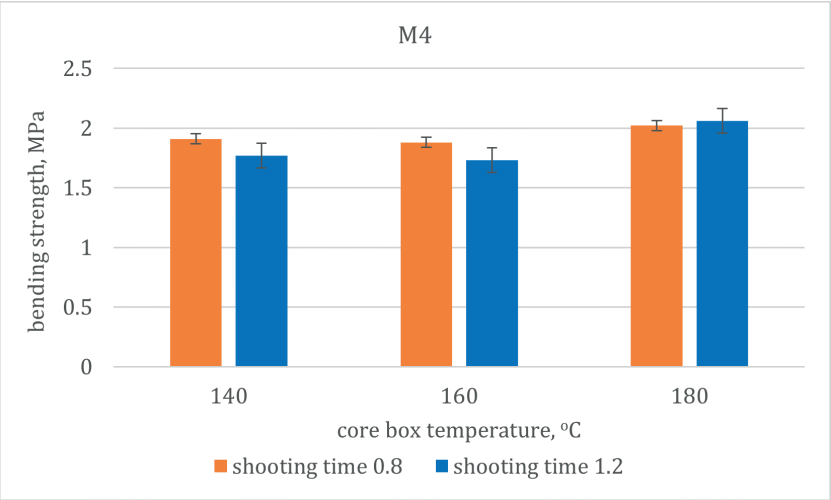

Fig. 4. The bending strength of standard specimens made from the core sand mixture (M4) containing 4.0 parts by weight of perlite ore as a function of the core box temperature and shooting time for the mixture

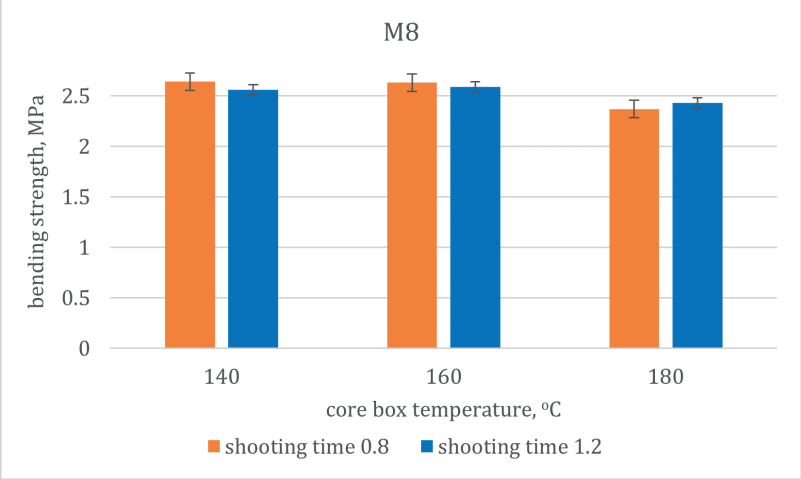

Fig. 5. The bending strength of standard specimens made from the core sand mixture (M8) containing 8.0 parts by weight of perlite ore as a function of the core box temperature and shooting time for the mixture

The core mixture containing 8.0 parts by mass of perlite ore exhibits better mechanical properties than the mixture with 4.0 parts by mass, but inferior to the mixture without the loosening additive. It should be noted that at core box temperatures of 140 and 160°C (Fig. 5), the obtained bending strength values are very similar, ranging between 2.56 and 2.64 MPa, with differences falling within the limits of statistical error.

For this core mixture, the lowest bending strength (approximately 2.4 MPa) was recorded at a core box temperature of 180°C. This is likely due to the physical process of solvent removal in the inorganic binder, which reduces its binding capacity. This confirms that such a binder performs best when cured at temperatures between 140 and 160°C. Further research should therefore focus on optimizing the holding time of samples in the core box, as increasing the temperature may only be justified if, when combined with a shorter holding time, it leads to higher production efficiency.

Figures 6 and 7 show the bending strength for all tested systems depending on the core box temperature, for two shooting times.

Figures 6 and 7 provide a summary and, at the same time, a more illustrative representation of the previous research results. They show that shooting time has no significant effect on the obtained bending strength values, regardless of whether the core mixture contains additives or not. As mentioned earlier, the increased specific surface area resulting from the introduction of an additional loose material (perlite ore) leads to a decrease in core strength, which is particularly evident for the M4 core mixture. With the same binder content (2.5 parts by mass), the M8 mixture (8.0 parts by mass of perlite ore) exhibited better mechanical properties at all tested core box temperatures. This may be attributed to the improved flowability of the core mixture, better compaction, and more uniform distribution of perlite ore grains, which are statistically larger and have a coarser main fraction compared to the base sand grains. The obtained results indicate the validity of optimizing the composition of the core mixture for each specific formulation and set of blowing process parameters.

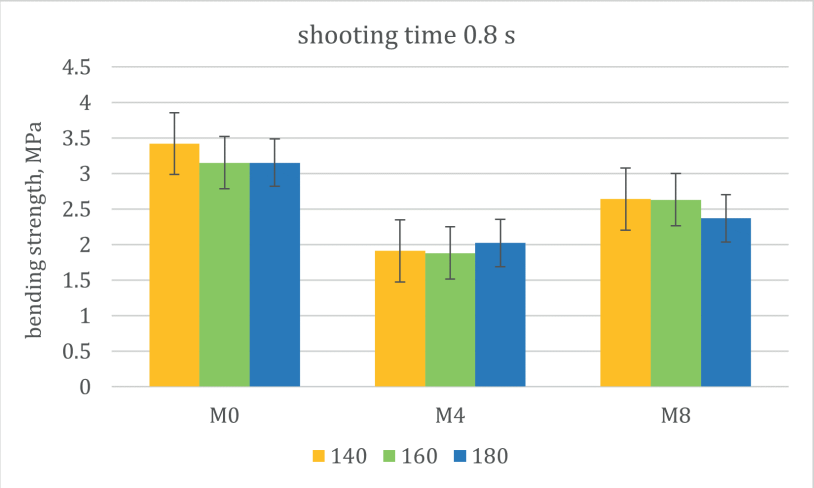

Fig. 6. Comparison of strength depending on core box temperature and shooting time of 0.8 s

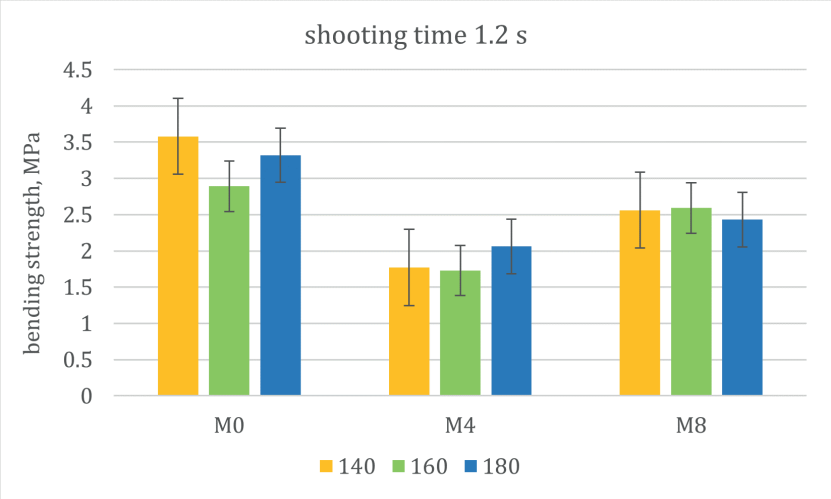

Fig. 7. Comparison of strength depending on core box temperature and shooting time of 1.2 s

4. CONCLUSIONS

The conducted research on the influence of a loosening additive in the form of perlite ore on the mechanical properties of cores produced by the warm-box process using an inorganic silicate binder has shown that:

- in the case of core mixtures prepared with the inorganic Cordis binder, increasing the core box temperature does not bring any benefits in terms of higher strength of standard cores (standard samples for bending strength testing) cured for 120 s. The best properties were obtained at temperatures of 140°C and 160°C, while increasing the temperature to 180°C may lead to the physical removal of the solvent from the binder, reducing its bonding ability;
- extending the shooting time results in increased strength only for the mixture without the addition of perlite ore. For the other tested systems (with 4.0 and 8.0 parts by mass of perlite ore), a decrease in strength was observed, which is due to a reduced flow rate of the core mixture from the shooting chamber and a lower concentration of the sand-air stream;
- with a constant binder content in the core mixture (2.5 parts by mass), the mixture containing 8.0 parts by mass of perlite ore exhibited better mechanical properties at all tested core box temperatures than the mixture with 4.0 parts by mass of perlite ore. This may be attributed to improved flowability and, consequently, a higher degree of compaction;
- the introduction of additives into molding and core sands requires case-by-case optimization of both the mixture composition and the blowing process parameters;
- the research will continue, focusing on determining the effects of binder type, grain size, and loosening additive, as well as the influence of operating pressure on the density and strength of cores in the core box. The amount of loosening additive introduced also requires optimization to achieve the desired improvement in core knockout properties.

ACKNOWLEDGMENTS

The research was conducted as part of the statutory work financed by the Ministry of Science and Higher Education, Poland: 16.16.170.654/B507.

REFERENCES

[1] Major-Gabryś K.A., Grabarczyk A., Dobosz S.M., Jakubski J., Morek J. & Beňo J. (2018). Measurement of molding sand elasticity. *Journal of Casting & Materials Engineering*, 2(2), 38–44. DOI: https://doi.org/10.7494/jcme.2018.2.2.38.

[2] Dańko R. & Jamrozowicz Ł. (2017). Density distribution and resin migration investigations in samples of sand core made by blowing method. *Journal of Casting & Materials Engineering*, 1(3), 70–73. DOI: https://doi.org/10.7494/jcme.2017.1.3.70.

[3] Dobosz S.M., & Major-Gabryś K. (2008). The mechanism of improving the knock-out properties of moulding sands with water glass. *Archives of Foundry Engineering,* 8(1), 37–42.

[4] Holtzer M., Drożyński D., Bobrowski A. & Plaza W. (2014). Influence of binding rates on strength properties of moulding sands with the GEOPOL binder. *Archives of Foundry Engineering*, 14(1), 37–40. DOI: https://doi.org/10.2478/afe-2014-0009.

[5] Bobrowski A., Holtze, M., Żymankowska-Kumon S. & Danko R. (2015). Harmfulness assessment of moulding sands with a geopolymer binder and a new hardener, in an aspect of the emission of substances from the BTEX Group. *Archives of Metallurgy and Materials*, 60(1), 341–344, https://doi.org/10.1515/amm-2015-0056.

[6] Izdebska-Szanda I., Żmudzińska M., Faber J. & Perszewska K. (2013). Aspekt ekologiczny mas formierskich z nowymi spoiwami nieorganicznymi w procesie zalewania form ciekłym metalem. *Prace Instytutu Odlewnictwa* LIII(4), 71–83. DOI: https://doi.org/10.7356/iod.2013.23.

[7] Izdebska-Szanda I. & Baliński A. (2011). New generation of ecological silicate binders. *Procedia Engineering,* 10, 887–893. DOI: https://doi.org/10.1016/j.proeng.2011.04.146.

[8] Izdebska-Szanda I., Kamińska J., Angrecki M., Palma A. & Stefański Z. (2017). The effect of additive "B" on the properties of foundry sands with hydrated sodium silicate made by Floster technology. *Archives of Foundry Engineering*, 17(2), 31–34. DOI: https://doi.org/10.1515/afe-2017-0046.

[9] Stachowicz M. & Granat K. (2013). Pochłanianie mikrofal przez nieutwardzone masy formierskie ze szkłem wodnym. *Archives of Foundry Engineering,* 13(Spec. Iss. 1), 169–174. URL: https://bibliotekanauki.pl/articles/379879 [25.10.2025].

[10] Stachowicz M., Granat K. & Małachowska A. (2014). Porównanie metod klasycznych i nowoczesnej mikrofalowej wytwarzania rdzeni z mas ze szkłem wodnym. *Archives of Foundry Engineering*, 14(Spec. Iss. 2), 83–88. URL: https://bibliotekanauki.pl/articles/381848 [25.10.2025].

[11] Dobosz S.M. & Major-Gabryś K. (2006). Samoutwardzalne masy ze szkłem wodnym i nowym utwardzaczem. *Inżynieria Materiałowa*, 27(3), 576–579.

[12] Granat K., Nowak D., Pigiel M., Stachowicz M. & Wikiera R. (2008). The influence of microwave heating and water glass kind on the properties of molding sands. *Archives of Foundry Engineering*, 8 (Spec. Iss. 1), 119–122.

[13] Granat K., Nowak D., Pigiel M., Stachowicz M. & Wikiera R. (2007). The influence of microwave curing time and water glass kind on the properties of molding sands. *Archives of Foundry Engineering*, 7(4), 79–82.

[14] Samar M. & Saxena S. (2016). Study of chemical and physical properties of perlite and its application in India. *International Journal of Science Technology and Management,* 5(4), 70–80. URL: https://www.ijstm.com/images/short_pdf/1460020555_434V.pdf [25.10.2025].

[15] Austin G.S., & Barker J.M. (1998). Commercial perlite deposits of New Mexico and North America. In: Mack G.H., Austin G.S., Barker & J.M. (Eds.), *Las Cruces Country II* , New Mexico Geological Society, 49th Annual Fall Field Conference Guidebook, pp. 271–277. DOI: https://doi.org/10.56577/FFC-49.271.

[16] Bagdassarov N., Ritter F. & Yane Y. (1999). Kinetics of perlite glasses degassing TG and DSC analysis. *Glass Science and Technology*, 72(9), 277–290.

[17] Derkowski A., Drits V.A. & McCarty D.K. (2012). Rehydration in a dehydrated-dehydroxylated smectite in environment of low water vapor content. *American Mineralogist,* 97(1), 110–127. DOI: https://doi.org/10.2138/am.2012.3872.

[18] Bobrowski A., Kaczmarska K., Sitarz M., Drożyński D., Leśniak M., Grabowska B. & Nowak D. (2021). Dehydroxylation of perlite and vermiculite: impact on improving the knock-out properties of moulding and core sand with an inorganic binder. *Materials*, 14(11), 2946. DOI: https://doi.org/10.3390/ma14112946.

[19] Inorganic sets the standard: Emission-free casting. URL: https://www.ha-group.com/en/products-and-services/products/inorganic-binder-systems/ [18.10.2025].

[20] Bobrowski A., Drożyński D. & Grabowska B. (2024). The influence of the matrix grain size and mineral addition on improving the knock-out properties of molding sands with an inorganic binder. *Applied Science*, 14(8), 3185. DOI: https://doi.org/10.3390/app14083185.

[21] Bobrowski A. (2018). *Zjawisko dehydroksylacji wybranych materiałów mineralnych z grupy glinokrzemianów jako czynnik determinujący poprawę wybijalności mas formierskich i rdzeniowych ze spoiwem nieorganicznym*. Wydawnictwo Archives of Foundry Engineering, Katowice-Gliwice.

[22] GEOPOL. https://www.geopol-info.com/ [18.10.2025].

[23] Uniwersalna maszyna do wykonywania próbek testowych i małych rdzeni w technologii Hot-Box, Cold-Box, Anorganik, CO_2. URL: https://multiserw-morek.pl/produkt/uniwersalna-maszyna-do-wykonywania-probek-testowych/ [18.10.2025].

[24] Supplier certificate. DB Cargo Polska. Piasek formierski 2K wg: PN-85 H-11001.

[25] Polska norma PN-85/H-11001: *Odlewnicze materiały formierskie – Kwarcowe piaski formierskie*.

[26] Urządzenie LRu-2e do badania wytrzymałości mas formierskich. URL: https://multiserw-morek.pl/produkt/urzadzenie-lru-2e-do-badania-wytrzymalosci-mas-formierskich/ [18.10.2025].

Journal of Casting & Materials Engineering Vol. 9 No. 4 (2025) 72–79
https://doi.org/10.7494/jcme.2025.9.4.72

Reverse Engineering and Computer Modelling in Archaeometallurgy for the Reconstruction of Heritage Objects Using Precision Casting and 3D Printing

Karolina Marlicka[a,*], Andrzej Fijołek[a], Aldona Garbacz-Klempka[a], Marcin Piękoś[a]

[a]AGH University of Krakow, Faculty of Foundry Engineering, 23 Reymonta St., 30 059 Krakow, Poland
**e-mail: marlicka@agh.edu.pl*

Received: 21 November 2025/Accepted: 17 December 2025/Published online: 23 December 2025.
This article is published with open access at AGH University of Science and Technology Journals

Abstract

This article presents an interdisciplinary approach to the reconstruction of a copper-alloy artefact using reverse engineering techniques combined with modern digital and manufacturing technologies. The research was motivated by the need to better understand historical casting techniques while preserving the integrity of cultural heritage objects through non-destructive methods. The study integrates 3D scanning, CAD-based modelling, numerical simulations, investment casting, and metal additive manufacturing.

The geometry of the artefact was captured using high-resolution 3D scanning, enabling the development of two CAD models: one representing the preserved state of the object and a second reconstructed model with the missing fragment digitally restored. Both models were used for numerical simulations of mould filling, solidification, cooling, and porosity formation performed in MAGMASOFT® 6.1, allowing the assessment of technological feasibility and defect formation. Based on the simulation results, physical replicas were produced using investment casting and selective laser melting.

The obtained numerical and experimental results were compared in terms of geometry reproduction, surface characteristics, and predicted versus observed casting behaviour. The study demonstrates that the combination of digital reconstruction, simulation tools, and experimental manufacturing provides a reliable framework for analysing historical metallurgical processes. The proposed methodology supports both scientific interpretation and the practical reconstruction of heritage objects and can be applied to a wide range of archaeometallurgical studies.

Keywords:

casting, additive manufacturing technologies, 3D scan, computer modelling, numerical simulations, copper alloys, bronze, selective laser melting, investment casting, cultural heritage, archaeometallurgy, reconstruction

1. INTRODUCTION

The reconstruction of historical metallurgical techniques requires the simultaneous consideration of material properties, geometry, and the processes associated with casting. Small metal objects preserve within their structure information relating to the mould, the dynamics of metal flow, and the technical conditions that accompanied their production. Contemporary research approaches rely on non-destructive analyses, 3D scanning, computer modelling, and numerical simulations, complemented by experimental casting and additive manufacturing technologies [1–7].

In this article, research on a single artefact made of a copper alloy is presented. The chemical composition of this type of alloy is characteristic of castings produced during the period from which the analysed object originates and falls within the range typical of historical foundry materials. Surface analysis revealed the presence of material loss and preserved corrosion products, which served as the basis for the development of a 3D model and a geometric reconstruction. These models were used to conduct numerical simulations of the filling and solidification processes, casting, and 3D printing, enabling a comprehensive comparison of various reconstruction pathways [5–8].

2. MATERIALS AND METHODS

The study was carried out using non-destructive methods, 3D scanning with CAD modelling, and modern casting and additive manufacturing processes. In the first stage, three-dimensional documentation of the artefact was performed using the Revopoint POP2 3D scanner, whose detailed technical specification is presented in Table 1. The scanning was conducted with the use of a rotary table, which enabled the acquisition of a high-density point cloud. The obtained data were processed in the Revo Scan 5 software, where the scan was cleaned, the fragments were aligned, and a triangular mesh was generated. Final, the 3D geometry of the examined casting was obtained [9].

Table 1
Specification of the Revopoint POP2 scanner (technical documentation provided by Revopoint)

Technology	Dual camera infrared light
Single-frame precision	Up to 0.05 mm
Single-frame accuracy	Up to 0.1 mm
Single capture range	210 mm × 130 mm
Working distance	150–400 mm
Minimum scan volume	20 mm × 20 mm × 20 mm
Scanning speed	Up to 10 fps
Light source	Class 1 infrared light
Alignment	Feature, marker
Point distance/resolution	0.15 mm

Based on the 3D scans, two models were developed in the SOLIDWORKS 2023 environment: a real model, reflecting the preserved state, and a reconstructed model, in which the missing fragment was supplemented. These models were used both for numerical simulations and for 3D printing. The 3D modelling included an analysis of wall thickness, reconstruction of the missing structure, and preparation of solid bodies consistent with the requirements of casting simulation software and the metal 3D printer.

Three-dimensional scanning enabled the reconstruction of the overall geometry of the object, including its characteristic proportions and approximate dimensions. To better illustrate the scale of the analysed artefact, a schematic drawing presenting the general dimensions of the object was prepared (Fig. 1).

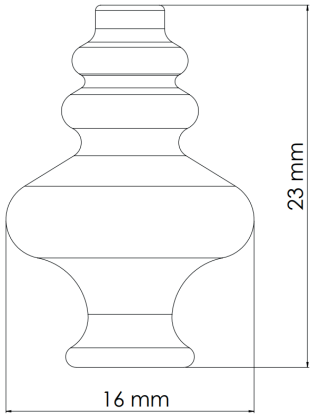

Fig. 1. Schematic drawing showing the approximate overall dimensions of the analysed object, prepared in SOLIDWORKS 2023

Numerical simulations of the mould filling, solidification, cooling, and porosity formation were carried out using the MAGMASOFT® 6.1 software. The simulations were based on previously prepared CAD models. For each model, appropriate functional roles were assigned within the simulation environment, and a virtual mould was generated, automatically adapting to the geometry of the casting.

The pouring parameters were defined individually for each object based on prior analyses. In the case of reconstructed forms, a CuSn12 alloy was applied, corresponding to one of the most commonly used bronze alloys in the Bronze Age. The pouring temperature was set to 1100°C in all simulations, ensuring optimal filling conditions for copper alloys. The pouring time was controlled by setting the filling level of the pouring basin to 70%, which enabled a stable metal flow and better reflected real casting conditions. The simulation results included temperature distribution after mould filling and predicted porosity distribution [2, 5].

The model intended for investment casting was exported to STL format and processed in CHITUBOX Basic V2.3, where the support system and model orientation were prepared. The replica was produced on an Elegoo Mars 3 3D printer using SuperCast-SuperFast (ENGR-A17L) photopolymer casting resin, designed for burnout processes in the investment casting technique. After completing the 3D printing, supports were removed and the model was cleaned, preparing it for moulding.

The mould was made using WiroFine refractory material, prepared in an AMX-1 vacuum mixer, which enabled thorough deaeration of the mass and ensured uniform consistency. The model was placed in metal cylinders, then filled with the refractory mass and left to solidify. The burnout and resin removal were carried out in an APE800 furnace in accordance with a predetermined temperature schedule: the mould was placed in a furnace preheated to 700°C, and the temperature was then increased by 50°C every 10 minutes, until reaching 1010°C, at which it was held for 60 minutes. This process enabled the complete burnout of the resin and the hardening of the ceramic shell [10, 11].

The casting was produced using the centrifugal method with a Pro-Dent WR02 casting centrifuge, which ensured the uniform filling of the mould with molten metal. The applied alloy was heated and melted in accordance with the technological parameters appropriate for this alloy system. After solidification, the ceramic mould was broken, and the casting was mechanically cleaned.

In parallel, a second technological replica was produced using metal 3D printing. The 3D model prepared in SOLIDWORKS 2023 was converted into a format compatible with a powder-bed printer and manufactured using the AL3D metal laser-sintering printer, employing the selective laser melting (SLM) method. The specification of the printer and the metal powder is also presented in Table 2. The additively manufactured reconstruction served to compare dimensional accuracy, surface characteristics, and potential differences resulting from alternative methods of producing low-mass objects with complex geometry [12–21].

Table 2
Specification of the AL3D printer (technical documentation provided by ALPHA LASER)

Process parameters	Open access to all machine and process parameters
Laser type	Fiber laser
Laser wave length	1,070 nm
Laser focal spot	0.05 mm
Laser scanning speed	Max. 5 m/s
Materials	m4p Brz10
Achievable component density	Up to 99%
Layer thickness	0.03 mm

The entire research procedure enabled the comparison of the geometry of the original object, the digital reconstruction, and the replicas produced using two different techniques, forming the basis for the further comparative analyses presented in subsequent chapters.

3. RESULTS

Surface observations revealed a visible metal loss with an irregular edge, as well as a depression covered with a greenish patina, which was left intact to preserve the structural integrity. The remaining surface areas showed features typical of small castings produced in moulds with characteristic micro-roughness.

3D scanning enabled precise reconstruction of the geometry, including variations in wall thickness in the damaged area. Figure 2 presents the CAD model of the preserved geometry, along with a magnification of the thinnest section. Figure 3 shows the reconstructed model, also with an enlarged view of the corresponding section, allowing for a direct comparison between the preserved state and the reconstruction.

Fig. 2. Model based on 3D scans developed in SOLIDWORKS 2023, with a close-up of a thin-walled section

Fig. 3. Reconstructed model developed in SOLIDWORKS 2023, with a close-up of a thin-walled section and the object's geometry reproduced

The transfer of both models into the MAGMASOFT® 6.1 software made it possible to perform numerical simulations. The filling of the scanned model, presented in Figure 4, proceeded smoothly, and the temperature distribution of the metal remained uniform. In subsequent stages of the filling process, no rapid temperature variations or indicating disturbances in the filling process were observed.

The solidification process of the scanned 3D model is shown in Figure 5. The temperature distribution progressed uniformly toward the gating system.

Analogous simulations were conducted for the reconstructed 3D model created in CAD software, where the filling behaviour shown in Figure 6, demonstrated nearly identical alloy behaviour compared to the scanned model. The solidification process, presented in Figure 7, progressed in accordance with the predicted pattern and remained consistent with the behaviour observed for the scanned model.

A comparative porosity analysis, the results of which are shown in Figure 8, indicated the presence of small porosity zones located in areas with characteristic geometric constrictions. In both models, a similar distribution of potential defects was predicted, resulting from local differences in solidification rates. At the same time, no concentrations of porosity were observed that could pose a significant threat to the structural integrity of the object during use.

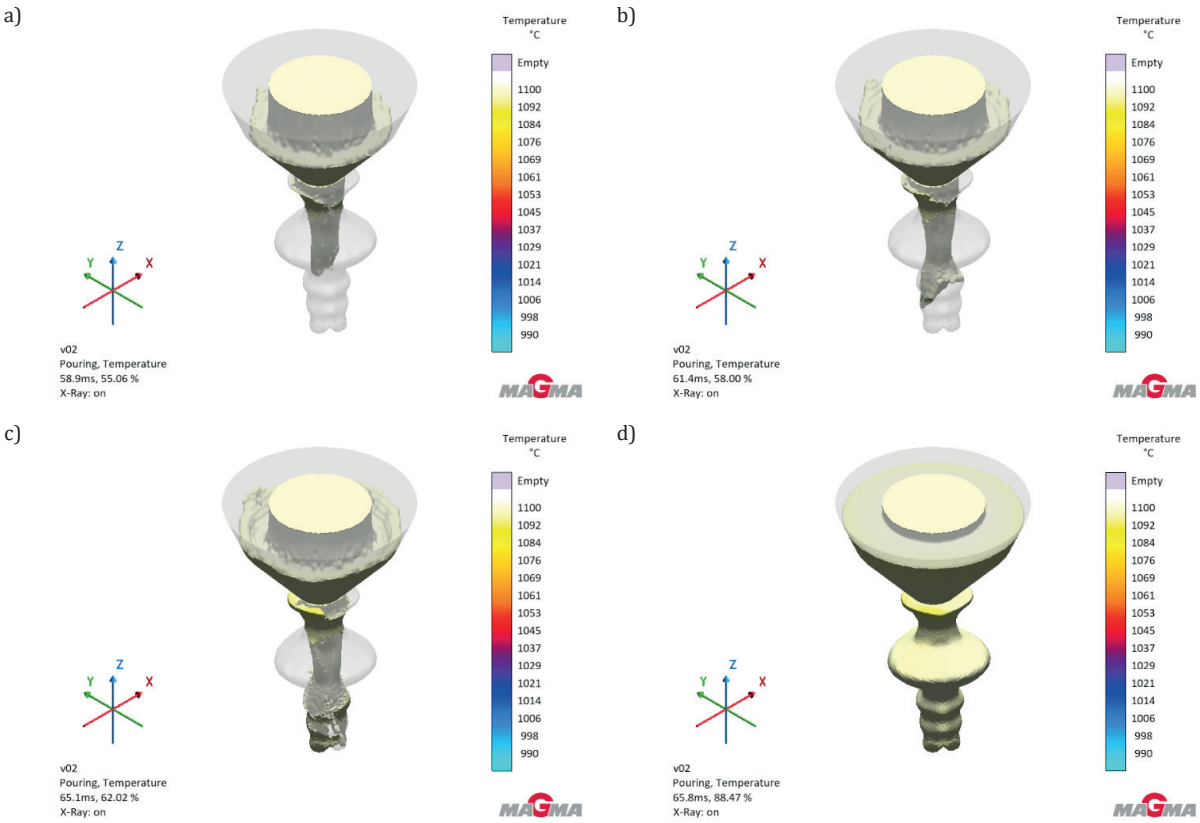

Fig. 4. Pouring simulation results in MAGMASOFT® 6.1 for the 3D scanned model at four stages of mould cavity filling: a) 55.06%; b) 58.00%; c) 62.02%; d) 88.47%

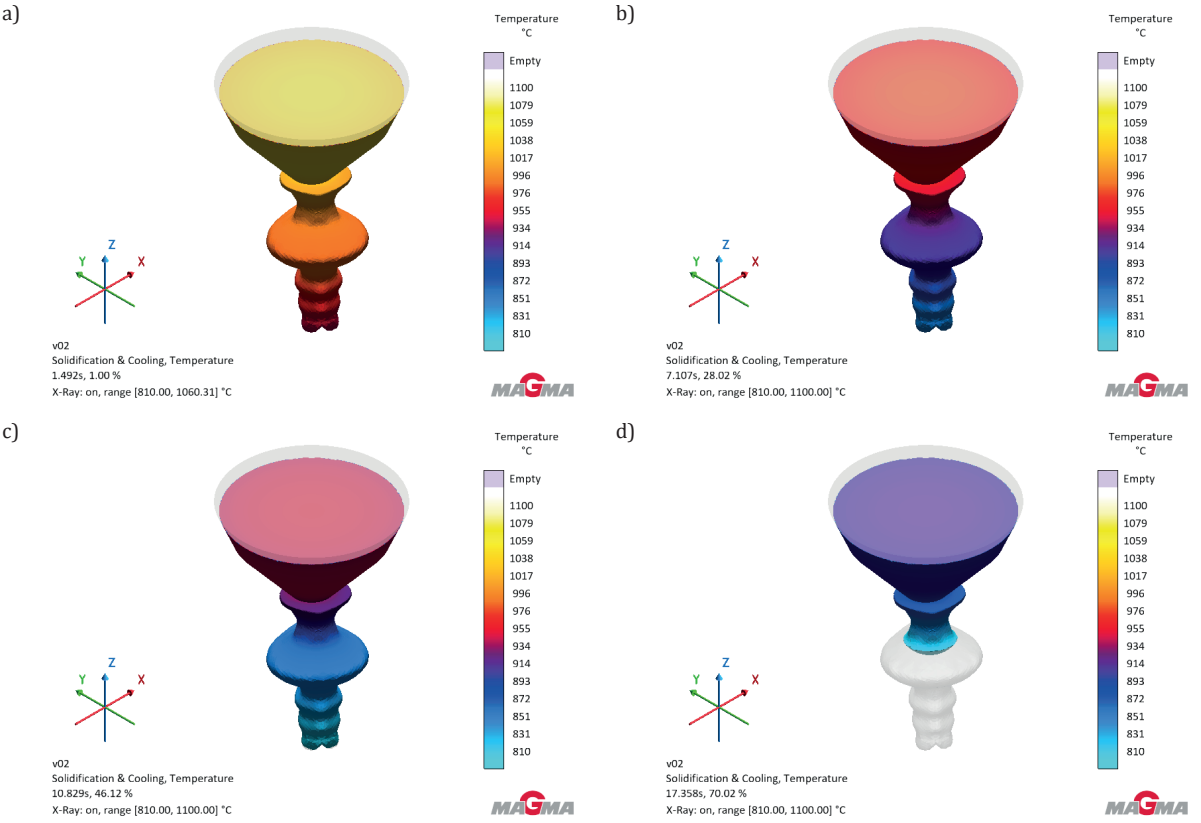

Fig. 5. Solidification simulation results in MAGMASOFT® 6.1 for the scanned model at four stages of mould cavity solidification: a) 1.00%; b) 28.02%; c) 46.12%; d) 70.02%

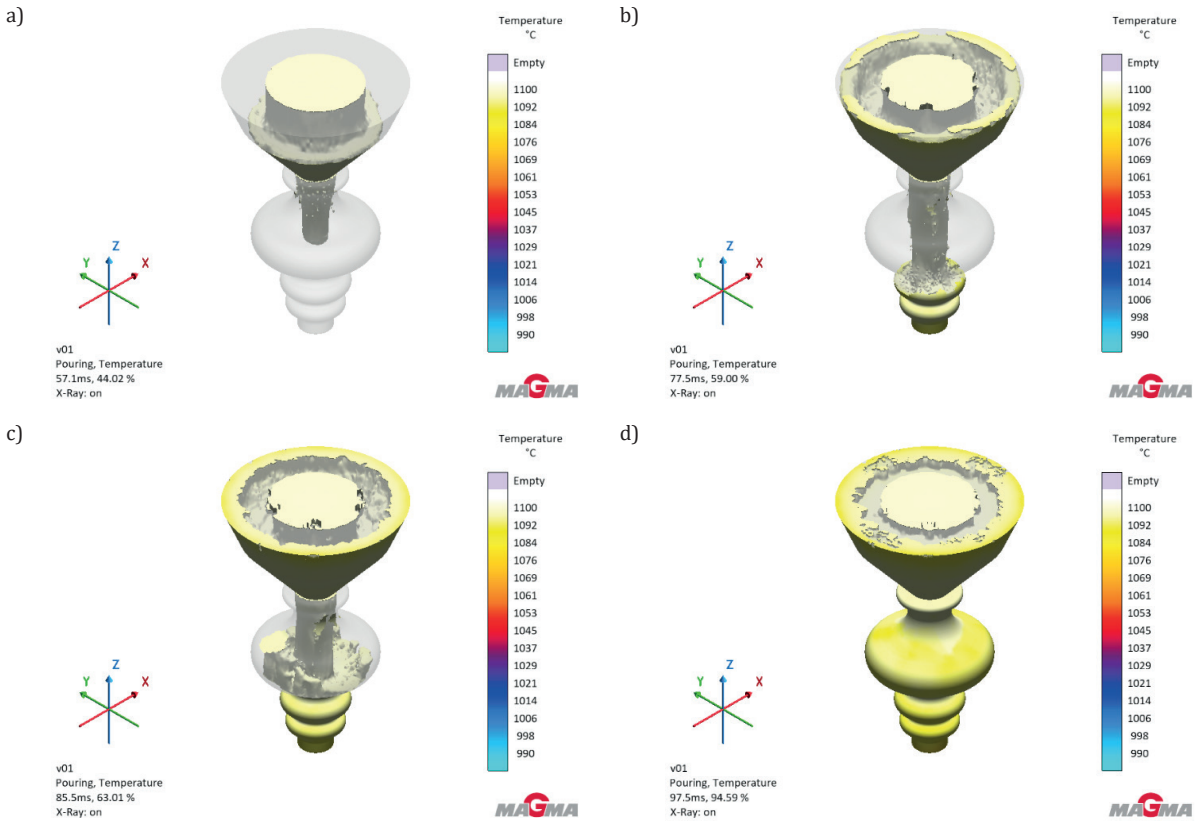

Fig. 6. Pouring simulation results in MAGMASOFT® 6.1 for the 3D CAD model at four stages of mould cavity filling: a) 44.02%; b) 59.00%; c) 63.01%; d) 94.59%

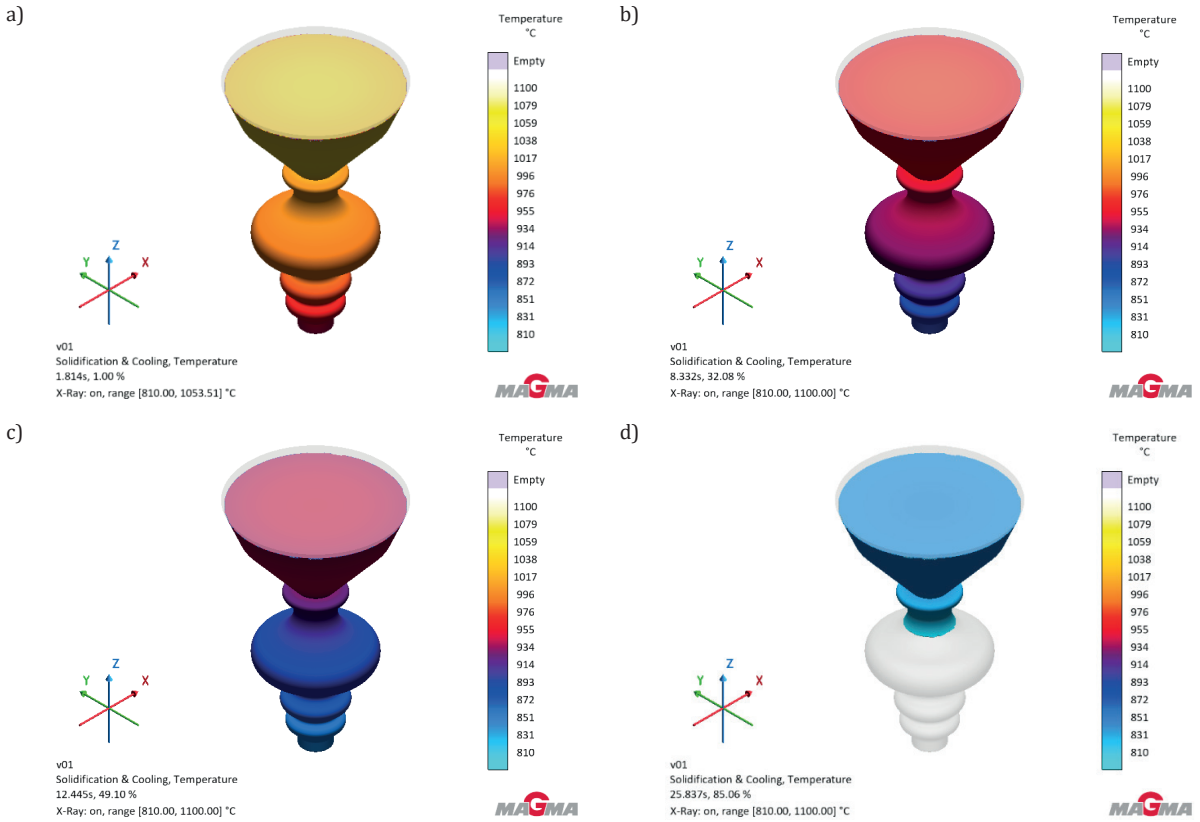

Fig. 7. Solidification simulation results in MAGMASOFT® 6.1 for the 3D CAD model at four stages of solidification process: a) 1.00%; b) 32.08%; c) 49.10%; d) 85.06%

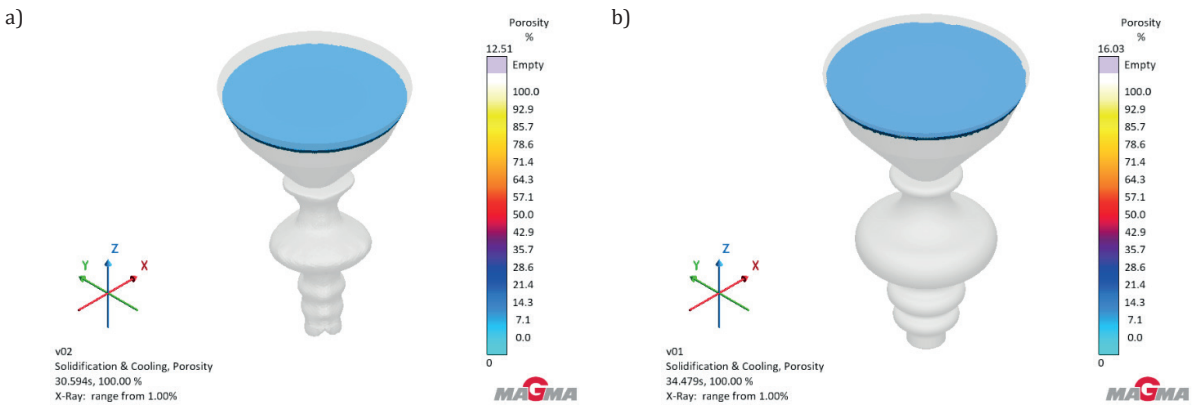

Fig. 8. Comparison of predicted porosity results in MAGMASOFT® 6.1 for the 3D scanned model (a) and the 3D CAD model (b)

The results of casting the modern replica of the object provided valuable comparative material, enabling the correlation of the numerical simulation predictions with the real behaviour of the copper alloy inside the ceramic mould. The model intended for casting, previously prepared in SOLIDWORKS 2023, was reproduced using 3D printing with photopolymer resin. The model obtained exhibited a smooth surface and high precision in detail reproduction, which was crucial for subsequent comparison with the original object and for reconstructing the thin-walled segments visible in the 3D scan.

The mould was prepared using a refractory mass, which, after initial setting, was subjected to resin burnout and ceramic shell heating, following a temperature schedule recommended by the manufacturer. After reaching the target temperature, the mould obtained the thermal and mechanical stability required to receive the molten metal.

The casting was produced using the centrifugal method with a casting centrifuge, which enabled rapid and uniform introduction of the CuSn12 copper alloy into the thin and complex regions of the mould cavity. During pouring, the alloy was introduced into the mould at a temperature close to that used in the simulations, ensuring the possibility of directly comparing the actual process course with the computational model. After cooling, the ceramic shell was removed, and the raw casting was mechanically cleaned.

The obtained casting, presented in Figure 9, exhibits characteristic surface features of castings produced using the investment casting method, including subtle differences resulting from the quality of the ceramic mass and the spinning parameters. The casting retained key geometrical features, enabling assessment of the consistency between the reconstruction model and the real metallurgical process. The thin-walled regions were reproduced without deformation, confirming that both the mould preparation and the metal flow dynamics in the centrifuge were consistent with the simulation predictions.

3D printing of the CAD model enabled comparison of geometric behaviour in an additive manufacturing process. The print obtained on the AL3D printer is presented in Figure 10. The model was faithfully reproduced, including the thin-walled segments, confirming the accuracy of the reconstruction and demonstrating the usefulness of 3D printing as an additional tool for assessing the geometry of the artefact. The printed model made it possible to analyse the proportions of the original form in physical space.

Fig. 9. Casting obtained using the investment casting method

Fig. 10. Object produced using a 3D printer

The obtained reconstruction enabled a comparison with the cast replica and the original object. Comparative analysis

of these three forms, the classical casting, the additively manufactured reconstruction, and the 3D scan data, allowed the identification of differences resulting from the manufacturing technologies and confirmed the usefulness of both techniques for reconstructing archaeometallurgical objects [22–24].

4. CONCLUSIONS

The conducted research confirmed that the use of integrated reconstruction methods, including 3D scanning, CAD-based modelling, casting simulations, 3D metal printing, and investment casting, allows for a comprehensive recreation of both the geometry and the potential manufacturing process of the analysed object. The obtained digital models demonstrated consistency with the predicted filling and solidification conditions, while the physical reconstructions further validated the technological assumptions. At the same time, the material characteristics of the artefact can be considered typical for castings of a similar origin, which situates it within the context of known metallurgical practices.

These studies highlight the importance of an interdisciplinary approach, where reverse engineering, digital tools, foundry techniques, and additive manufacturing technologies complement each other, creating a coherent reconstruction model. The results obtained represent one stage of a longer research process conducted at the Historical Layers Research Centre AGH, where the object was analysed and where the subsequent stages of the project are being carried out. Further work is planned, including additional comparisons of reconstructions, an expanded analysis of simulation parameters, and testing of alternative technological variants. This will enable an even more complete reconstruction of the object's production process and a better understanding of the relationships between its geometry, material, and historical casting technique.

ACKNOWLEDGMENTS

The work was funded under the European Funds for a Modern Economy 2021–2027 programme FENG 2.4 Badawcza Infrastruktura Nowoczesnej Gospodarki FENG.02.04-IP.04-001/24 MAPA pt. Polska infrastruktura dla badań nad dziedzictwem kulturowym – ERIHS.PL, conducted at the AGH University of Science and Technology. The provided funding enabled the use of modern, interdisciplinary methods of analysis and reconstruction, which were essential for the comprehensive elaboration of the results presented in this article.

REFERENCES

[1] Garbacz-Klempka A., Rosołowski S., Gackowski J., Wardas-Lasoń M., Dąbrowski H. P., Fijołek A., Piękoś M., Kozana J., Tabaszewski W., Jurecki P., Wałach D., Kaczmarczyk G. & Marlicka K. (2024). Wytwórczość brązownicza w grodzie kultury łużyckiej w Biskupinie w świetle wyników badań archeometalurgicznych. In: *90. rocznica rozpoczęcia badań wykopaliskowych w Biskupinie: jubileuszowa Konferencja Naukowa: 7–8 listopada 2024.* Biskupin: Muzeum Archeologiczne.

[2] Fijołek A., Garbacz-Klempka A., Wardas-Lasoń M., Marlicka K., Piekło J., Piękoś M., Kozana J. & Wałach D. (2025). Archaeometallurgy using modern research techniques and reverse engineering. Results obtained and prospects for the future. In: *ICME 25: V International Conference of Casting and Materials Engineering: Lightweight Innovations for a Better Climate: Krakow, Poland, October 27–28, 2025*. Krakow: AGH University of Krakow, Faculty of Foundry Engineering.

[3] Garbacz-Klempka A., Suchy J. S., Kwak Z., Długosz P. & Stolarczyk T. (2018). Casting technology experiment and computer modeling of ornaments from Bronze Age. *Archives of Metallurgy and Materials*, 63(3), 1329–1337. DOI: https://doi.org/10.24425/123808.

[4] Garbacz-Klempka A., Piękoś M., Perek-Nowak M., Kozana J., Żak P., Fijołek A., Silska P. & Stróżyk M. (2022). Reconstruction of the Late Bronze Age foundry process in Greater Poland: Analyses and simulations. Case study of hoard from Przybysław. *Archives of Metallurgy and Materials*, 67(3), 1125–1136. DOI: https://doi.org/10.24425/amm.2022.139712.

[5] Garbacz-Klempka A., Kwak Z., Żak P. L., Szucki M., Ścibior D., Stolarczyk T. & Nowak K. (2017). Reconstruction of the casting technology in the Bronze Age on the basis of investigations and visualisation of casting moulds. *Archives of Foundry Engineering*, 17(3), 184–190. DOI: https://doi.org/10.1515/afe-2017-0113.

[6] Garbacz-Klempka A., Rzadkosz S., Stolarczyk T., Piękoś M. & Kozana J. (2013). Archaeological remains of the copper metallurgy in Lower Silesia. *Metallurgy and Foundry Engineering*, 39(2), 29–36. DOI: https://doi.org/10.7494/mafe.2013.39.2.29.

[7] Liu B., Zhang F., Sun X. & Rushworth A. (2023). Additive manufacturing in cultural heritage preservation and product design. In: Pei E., Bernard A., Gu D., Klahn Ch., Monzón M., Petersen M., Sun T. (Eds.), *Springer Handbook of Additive Manufacturing*. Cham: Springer International Publishing, pp. 923–940.

[8] Cleary P., Ha J., Alguine V. & Nguyen T. (2002). Flow modelling in casting processes. *Applied Mathematical Modelling*, 26(2), 171–190. DOI: https://doi.org/10.1016/S0307-904X(01)00054-3.

[9] Prochaska M. & Mitka B. (2016). RevoScan – automatic device for 3D digitisation: Concept, application, test results. *Geomatics and Environmental Engineering*, 10(4), 81–87. DOI: https://doi.org/10.7494/geom.2016.10.4.81.

[10] Davey C.J. (2009). The early history of lost-wax casting. In: Mei J., Rehren T. (Eds.), *Metallurgy and Civilisation: Eurasia and Beyond*. London: Archetype Publications, pp. 147–154.

[11] Hunt B.L. (1980). The long history of lost wax casting: Over five thousand years of art and craftsmanship. *Gold Bulletin*, 13(2), 63–79. DOI: https://doi.org/10.1007/BF03215456.

[12] Kantaros A., Ganetsos T. & Petrescu F.I.T. (2023). Three-dimensional printing and 3D scanning: Emerging technologies exhibiting high potential in the field of cultural heritage. *Applied Sciences*, 13(8), 4777. DOI: https://doi.org/10.3390/app13084777.

[13] Bašić A., Mladineo M., Peko I. & Aljinović Meštrović A. (2018). 3D scanning, CAD optimization and 3D print application in cultural heritage: An example on statue from the ancient Salona. In: *8th International Conference "Mechanical Technologies and Structural Materials 2018", Split, Croatia, 27–28 September 2018*.

[14] Balletti C., Ballarin M. & Guerra F. (2017). 3D printing: State of the art and future perspectives. *Journal of Cultural Heritage*, 26, 172–182. DOI: https://doi.org/10.1016/j.culher.2017.02.010.

[15] Elias C. (2019). Whose digital heritage? Contemporary art, 3D printing and the limits of cultural property. *Third Text*, 33(6), 687–707. DOI: https://doi.org/10.1080/09528822.2019.1667629.

[16] Parfenov V., Igoshin S., Masaylo D., Orlov A. & Kuliashou D. (2022). Use of 3D laser scanning and additive technologies for reconstruction of damaged and destroyed cultural heritage objects. *Quantum Beam Science*, 6(1), 11. DOI: https://doi.org/10.3390/qubs6010011.

[17] Duda T. & Raghavan L. V. (2016). 3D metal printing technology. *IFAC-PapersOnLine*, 49(29), 103–110. DOI: https://doi.org/10.1016/j.ifacol.2016.11.111.

[18] Sadiq Al-Baghdadi M.A.R. (2017). 3D printing and 3D scanning of our ancient history: Preservation and protection of our cultural heritage and identity. *International Journal of Energy and Environment*, 8(5), 441–456.

[19] Nancharaiah T. (2020). A review paper on metal 3D printing technology. In: Patnaik A., Kozeschnik E., Kukshal V. (Eds.), *Advances in Materials Processing and Manufacturing Applications. Proceedings of iCADMA 2020*, Springer, pp. 251–259. DOI: https://doi.org/10.1007/978-981-16-0909-1_25.

[20] Konda Gokuldoss P., Kolla S. & Eckert J. (2017). Additive manufacturing processes: Selective laser melting, electron beam melting and binder jetting – Selection guidelines. *Materials*, 10(6), 672. DOI: https://doi.org/10.3390/ma10060672.

[21] Sefene E.M. (2022). State-of-the-art of selective laser melting process: A comprehensive review. *Journal of Manufacturing Systems*, 63, 250–274. DOI: https://doi.org/10.1016/j.jmsy.2022.04.002.

[22] Scudino S., Unterdörfer C., Prashanth K.G., Attar H., Ellendt N., Uhlenwinkel V. & Eckert J. (2015). Additive manufacturing of Cu–10Sn bronze. *Materials Letters*, 156, 202–204. DOI: https://doi.org/10.1016/j.matlet.2015.05.076.

[23] Padovezzi R.O., Garcia Trindade W., Marques G.A., Pereira Gomes Pinto E., Costa Silva M., Amorese R.A., Santos Damasio T. & Tedardi do Nascimento P.H. (2025). Effects of the additive manufacturing process on the mechanical and structural properties of bronze alloys: A review. *Revista de Gestão e Secretariado*, 16(7), 5057–5057. DOI: https://doi.org/10.7769/gesec.v16i7.5057.

[24] Rahmani R., Resende P.R., Couto R., Lopes S.I., Kumar R., Maurya H.S., Karimi J, Afonso A.M., Hussain A. & Abrantes J.C.C (2024). Structural analysis of selective laser melted copper-tin alloy. *Journal of Alloys and Metallurgical Systems*, 7, 100097. DOI: https://doi.org/10.1016/j.jalmes.2024.100097.